Mon. Not. R. Astron. Soc. **394,** 978–994 (2009) doi:10.1111/j.1365-2966.2008.14378.x

Post-common-envelope binaries from SDSS – V. Four eclipsing white dwarf main-sequence binaries

S. Pyrzas,[1,2⋆] B. T. Gänsicke,[1] T. R. Marsh,[1] A. Aungwerojwit,[1,3] A. Rebassa-Mansergas,[1] P. Rodríguez-Gil,[2,4] J. Southworth,[1] M. R. Schreiber,[5] A. Nebot Gomez-Moran[6] and D. Koester[7]

[1]*Department of Physics, University of Warwick, Coventry CV4 7AL*
[2]*Isaac Newton Group of Telescopes, Apartado de correos 321, S/C de la Palma E-38700, Canary Islands, Spain*
[3]*Department of Physics, Faculty of Science, Naresuan University, Phitsanulok 65000, Thailand*
[4]*Instituto de Astrofísica de Canarias, Vía Láctea, s/n, La Laguna E-38205, Tenerife, Spain*
[5]*Departamento de Fisica y Astronomia, Universidad de Valparaiso, Avenida Gran Bretana 1111, Valparaiso, Chile*
[6]*Astrophysikalisches Institut Potsdam, An der Sternwarte 16, D-14482 Potsdam, Germany*
[7]*Institut für Theoretische Physik und Astrophysik, University of Kiel, 24098 Kiel, Germany*

Accepted 2008 December 11. Received 2008 December 2; in original form 2008 November 4

ABSTRACT

We identify SDSS 011009.09+132616.1, SDSS 030308.35+005444.1, SDSS 143547.87+373338.5 and SDSS 154846.00+405728.8 as four eclipsing white dwarf plus main-sequence (WDMS) binaries from the Sloan Digital Sky Survey (SDSS), and report on follow-up observations of these systems. SDSS 0110+1326, SDSS 1435+3733 and SDSS 1548+4057 contain DA white dwarfs, while SDSS 0303+0054 contains a cool DC white dwarf. Orbital periods and ephemerides have been established from multiseason photometry. SDSS 1435+3733, with $P_{\rm orb} = 3$ h has the shortest orbital period of all known eclipsing WDMS binaries. As for the other systems, SDSS 0110+1326 has $P_{\rm orb} = 8$ h, SDSS 0303+0054 has $P_{\rm orb} = 3.2$ h and SDSS 1548+4057 has $P_{\rm orb} = 4.4$ h. Time-resolved spectroscopic observations have been obtained and the Hα and Ca II $\lambda\lambda$8498.02, 8542.09, 8662.14 triplet emission lines, as well as the Na I $\lambda\lambda$8183.27, 8194.81 absorption doublet were used to measure the radial velocities of the secondary stars in all four systems. A spectral decomposition/fitting technique was then employed to isolate the contribution of each of the components to the total spectrum, and to determine the white dwarf effective temperatures and surface gravities, as well as the spectral types of the companion stars. We used a light-curve modelling code for close binary systems to fit the eclipse profiles and the ellipsoidal modulation/reflection effect in the light curves, to further constrain the masses and radii of the components in all systems. All three DA white dwarfs have masses of $M_{\rm WD} \sim 0.4$–$0.6\,{\rm M}_{\odot}$, in line with the expectations from close binary evolution. The DC white dwarf in SDSS 0303+0054 has a mass of $M_{\rm WD} \gtrsim 0.85\,{\rm M}_{\odot}$, making it unusually massive for a post-common-envelope system. The companion stars in all four systems are M dwarfs of spectral type M4 and later. Our new additions raise the number of known eclipsing WDMS binaries to 14, and we find that the average white dwarf mass in this sample is $\langle M_{\rm WD}\rangle = 0.57 \pm 0.16\,{\rm M}_{\odot}$, only slightly lower than the average mass of single white dwarfs. The majority of all eclipsing WDMS binaries contain low-mass ($<0.6\,{\rm M}_{\odot}$) secondary stars, and will eventually provide valuable observational input for the calibration of the mass–radius relations of low-mass main-sequence stars and of white dwarfs.

Key words: binaries: close – binaries: eclipsing – stars: fundamental parameters – stars: late-type – white dwarfs.

⋆E-mail: s.pyrzas@warwick.ac.uk

1 INTRODUCTION

White dwarfs and low-mass stars represent the most common types of stellar remnant and main-sequence star, respectively, encountered in our Galaxy. Yet, despite being very common, very few white dwarfs and low-mass stars have accurately determined radii and masses. Consequently, the finite temperature mass–radius relation of white dwarfs (e.g. Wood 1995; Panei, Althaus & Benvenuto 2000) remains largely untested by observations (Provencal et al. 1998). In the case of low-mass stars, the empirical measurements consistently result in radii up to 15 per cent larger and effective temperatures 400 K or more below the values predicted by theory (e.g. Ribas 2006; López-Morales 2007). This is most clearly demonstrated using low-mass eclipsing binary stars (Bayless & Orosz 2006), but is also present in field stars (Berger et al. 2006; Morales, Ribas & Jordi 2008) and the host stars of transiting extrasolar planets (Torres 2007).

Eclipsing binaries are the key to determine accurate stellar masses and radii (e.g. Andersen 1991; Southworth & Clausen 2007). However, because of their intrinsic faintness, very few binaries containing white dwarfs and/or low-mass stars are currently known. Here, we report the first results of a programme aimed at the identification of eclipsing white dwarf plus main-sequence (WDMS) binaries, which will provide accurate empirical masses and radii for both types of stars. Because short-period WDMS binaries underwent common envelope (CE) evolution, they are expected to contain a wide range of white dwarf masses, which will be important for populating the empirical white dwarf mass–radius relation. Eclipsing WDMS binaries will also be of key importance in filling in the mass–radius relation of low-mass stars at masses $\lesssim 0.6\,\mathrm{M}_{\odot}$.

The structure of the paper is as follows. The target selection for this programme is described in Section 2. In Section 3 we present our observations and data reduction in detail. We determine the orbital periods and ephemerides of the four eclipsing WDMS binaries in Section 4, and measure the radial velocities of the secondary stars in Section 5. In Section 6 we derive initial estimates of the stellar parameters from fitting the Sloan Digital Sky Survey (SDSS) spectroscopy of our targets. Basic equations for the following analysis are outlined in Section 7. In Section 8 we describe our fits to the observed light curves, and present our results in Section 9. The past and future evolution of the four stars is explored in Section 10. Finally, we discuss and summarize our findings, including an outlook on future work in Section 11.

2 TARGET SELECTION

We have selected eclipsing SDSS WDMS binaries based on the available information on the radial velocities of their companion stars, and/or evidence of a strong reflection effect.

Initially, we used SDSS spectroscopy to measure the radial velocity of the companion star either from the Na I λλ8183.27, 8194.81 absorption doublet, or from the Hα emission line (see Rebassa-Mansergas et al. 2007 for details). SDSS J030308.35+005444.1 (henceforth SDSS 0303+0054) and SDSS J143547.87+373338.6 (henceforth SDSS 1435+3733) exhibited the largest secondary star radial velocities among ∼1150 WDMS binaries which have SDSS spectra of sufficiently good quality, 287 and 335 km s^{-1}, respectively. For SDSS J011009.09+132616.1 (henceforth SDSS 0110+1326) two SDSS spectra are available, which differ substantially in the strength of the emission lines from the heated companion star. Photometric time series (Section 3) revealed white dwarf eclipses in all three objects. SDSS 1435+3733 has been independently identified as an eclipsing WDMS binary by Steinfadt, Bildsten & Howell (2008).

Table 1. Full SDSS names and u, g, r, i, z magnitudes of SDSS 0110+1326, SDSS 0303+0054, SDSS 1435+3733 and SDSS 1548+4057.

SDSS J	u	g	r	i	z
011009.09+132616.1	16.51	16.53	16.86	17.02	16.94
030308.35+005444.1	19.14	18.60	18.06	16.89	16.04
143547.87+373338.5	17.65	17.14	17.25	16.98	16.66
154846.00+405728.8	18.79	18.32	18.41	18.17	17.68

As the number of SDSS WDMS binaries with known orbital periods, $P_{\rm orb}$, and radial velocity amplitudes, $K_{\rm sec}$, is steadily growing (Rebassa-Mansergas et al. 2008; Schreiber et al. 2008), we are now in the position to further pinpoint the selection of candidates for eclipses: with $P_{\rm orb}$ and $K_{\rm sec}$ from our time-series spectroscopy, and $M_{\rm WD}$ and $M_{\rm sec}$ from our spectral decomposition/fitting of the SDSS spectra (Rebassa-Mansergas et al. 2007), we can estimate the binary inclination from Kepler's third law. In the case of SDSS J154846.00+405728.8 (henceforth SDSS 1548+4057), the available information suggested $i \sim 85^{\circ}$, and time-series photometry confirmed the high inclination through the detection of eclipses.

Full coordinates and SDSS u, g, r, i, z point spread function magnitudes of the four systems are given in Table 1.

3 OBSERVATIONS AND DATA REDUCTION

Follow-up observations of the four systems – time series CCD photometry and time-resolved spectroscopy – were obtained at five different telescopes, namely the 4.2-m William Herschel Telescope (WHT), the 2.5-m Nordic Optical Telescope (NOT), the 2.2-m telescope in Calar Alto (CA2.2), the 1.2-m Mercator telescope (MER) and the IAC 0.8 m (IAC80). A log of the observations is given in Table 2, while Fig. 1 shows phase-folded light curves and radial velocity curves of all the systems. A brief account of the used instrumentation and the data reduction procedures is given below.

3.1 Photometry

Photometric observations of the four targets were obtained at all five telescopes. In every telescope set-up, care has been taken to ensure that at least three good comparison stars were available in the science images, especially in the cases when the CCDs were windowed.

3.1.1 WHT 4.2 m

The observations were carried out using the AUX-port imager, equipped with the default 2148 × 4200 pixel E2V CCD44-82 detector, with an unvignetted, circular field-of-view (FOV) of 2.2 arcmin in diameter. For the observations, the CCD was binned (4 × 4) to reduce readout time to 4 s. SDSS 1548+4057 was observed with a Johnson R filter. The images were debiased and flat-fielded within MIDAS and aperture photometry was carried out using SEXTRACTOR (Bertin & Arnouts 1996). A full account of the employed reduction pipeline is given by Gänsicke et al. (2004).

3.1.2 NOT 2.5 m

The observations were carried out using the Andalucia Faint Object Spectrograph and Camera (ALFOSC), equipped with a

Table 2. Log of the observations.

Date	Obs.	Filter/grating	Exp. (s)	Frames	Eclipses
SDSS 0110+1326					
2006 August 4	IAC80	*I*	420	25	0
2006 August 5	IAC80	*I*	60	170	0
2006 August 10	IAC80	*I*	420	13	0
2006 August 15	IAC80	*I*	420	15	0
2006 August 16	IAC80	*I*	420	12	0
2006 September 15	CA2.2	*I*	60	130	1
2006 September 16	CA2.2	*I*	45–55	312	1
2006 September 17	CA2.2	*I*	25–60	582	1
2006 September 26	WHT	R600B/R316R	1200	2	
2006 September 27	WHT	R600B/R316R	600	4	
2006 September 29	WHT	R600B/R316R	600	2	
2007 August 20	CA2.2	*BV*	25	159	0
2007 August 21	CA2.2	*BV*	25	101	0
2007 September 3	WHT	R1200B/R600R	1000	2	
2007 September 4	WHT	R1200B/R600R	1000	4	
2007 October 9	MER	Clear	40	150	1
SDSS 0303+0054					
2006 September 12	CA2.2	Clear	15–35	443	1
2006 September 14	CA2.2	Clear	45–60	63	1
2006 September 15	CA2.2	Clear	60	44	1
2006 September 18	CA2.2	*R*	50–60	165	1
2006 September 26	WHT	R600B/R316R	600	4	
2006 September 27	WHT	R600B/R316R	600	18	
2007 August 22	CA2.2	*BV*	30	63	1
2007 August 26	CA2.2	*BV*	35	84	1
2007 October 15	MER	Clear	55	60	1
SDSS 1435+3733					
2006 July 4	WHT	R1200B/R600R	720	1	
2006 July 5	WHT	R1200B/R600R	900	1	
2007 February 16	IAC80	*I*	90	45	1
2007 February 17	IAC80	*I*	90	162	1
2007 February 18	IAC80	*I*	70	226	2
2007 May 18	CA2.2	*V*	15	9	1
2007 May 19	CA2.2	*BV*	12	48	1
2007 May 19	CA2.2	Clear	12–15	27	1
2007 June 23	WHT	R1200B/R600R	1200	5	
2007 June 24	WHT	R1200B/R600R	1200	2	
SDSS 1548+4057					
2006 July 2	WHT	R1200B/R600R	1200	1	
2006 July 3	WHT	R1200B/R600R	1500	1	
2007 June 19	WHT	R1200B/R600R	1200	3	
2007 June 20	WHT	R1200B/R600R	1200	2	
2007 June 21	WHT	R1200B/R600R	1200	4	
2007 June 22	WHT	R1200B/R600R	1200	4	
2007 June 23	WHT	R1200B/R600R	1200	1	
2007 June 24	WHT	R1200B/R600R	1200	2	
2008 May 8	IAC80	*V*	300	71	1
2008 May 10	IAC80	*R*	300	64	2
2008 May 12	IAC80	*R*	300	5	1
2008 June 26	NOT	Clear	140	60	1
2008 June 29	NOT	Clear	30	90	1
2008 July 5	WHT	*R*	5	247	1

2k × 2k pixel E2V CCD42-40 chip, with a FOV of 6.5 × 6.5 arcmin^2. The CCD was binned (2 × 2) to reduce readout time. Filterless observations were obtained for SDSS 1548+4057. The reduction procedure for the NOT data was the same as the one used for the WHT data.

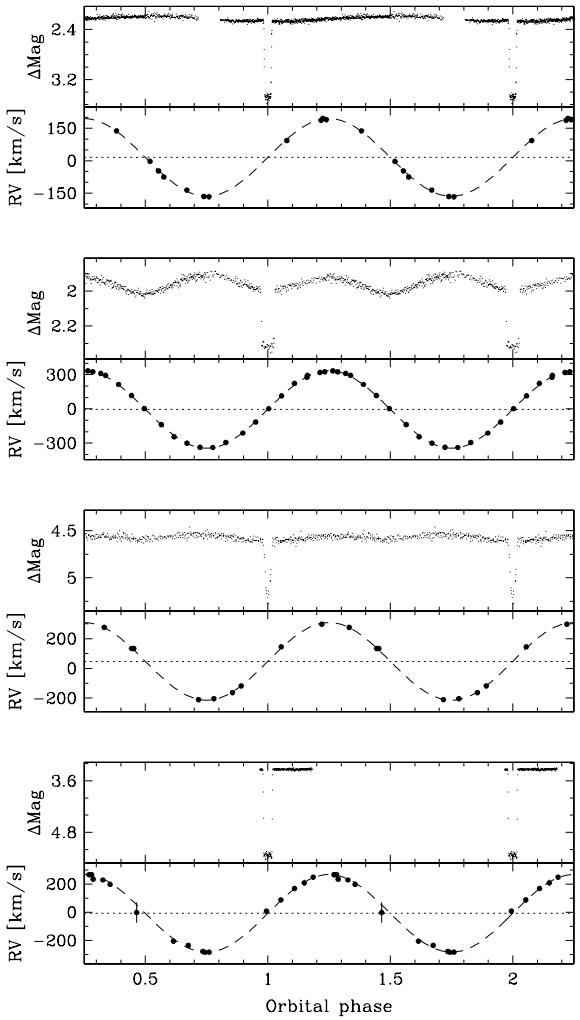

Figure 1. Phase-folded light- and radial velocity curves of the four systems. From top to bottom (two panels for each system): CA2.2 *I*-band light curve and Ca II radial velocity curve of SDSS 0110+1326, CA2.2 filterless light curve and Na I radial velocity curve of SDSS 0303+0054, IAC80 *I*-band light curve and Na I radial velocity curve of SDSS 1435+3733 and WHT *R*-band light curve and Na I radial velocity curve of SDSS 1548+4057.

3.1.3 Calar Alto 2.2 m

The observations were carried out using the Calar Alto Faint Object Spectrograph (CAFOS) equipped with the standard 2k × 2k pixel SITe CCD (FOV 16 × 16 arcmin^2). For the observations, the CCD was windowed to reduce readout time to 10 s. Observations were carried out using Johnson V, R, I and 'Röser' BV[1] filters, as well as without any filter. In detail, we used *I* and *BV* for SDSS 0110+1326, *R* and *BV* for SDSS 0303+0054 and *V*, *BV* and no filter for SDSS 1435+3733. The reduction procedure was the same as described above.

3.1.4 Mercator 1.2 m

Filterless photometric observations have been obtained for SDSS 0110+1326 and SDSS 0303+0054 using the Mercator

[1] A BG39/3 filter centred on 4977 Å with a full width at half-maximum (FWHM) of 1559 Å.

Optical Photometric Imager (MEROPE) equipped with a 2k × 2k EEV CCD chip (FOV 6.5 × 6.5 arcmin^2). For the observations, the CCD was binned (3 × 3) to reduce readout time to about 8 s. The reduction procedure for the Mercator data was the same as above.

3.1.5 IAC 0.8 m

Johnson *I*-band photometry has been obtained at the IAC 0.8-m telescope for SDSS 0110+1326 and SDSS 1435+3733, while *V*- and *R*-band photometry has been obtained for SDSS 1548+4057. The telescope was equipped with the SI 2k × 2k E2V CCD (FOV 10.25 × 10.25 arcmin^2), which was binned (2 × 2) and windowed to reduce readout time to 11 s. Data reduction was performed within IRAF.[2] After bias and flat-field corrections the images were aligned and instrumental magnitudes were measured by means of aperture photometry.

3.2 Spectroscopy

All spectroscopy presented in this work was acquired using the WHT and the Intermediate dispersion Spectrograph and Imaging System (ISIS). For the red arm the grating used was either R316R or R600R, and for the blue arm the grating was either R600B or R1200B. For all observations the blue-arm detector was an EEV 2k × 4k CCD. In 2006 July and September the red-arm detector was a Marconi 2k × 4k CCD, and in later observing runs a high-efficiency RED+ 2k × 4k CCD was used. In all cases the CCDs were binned spectrally by a factor of 2 and spatially by factors of 2–4, to reduce readout noise, and windowed in the spatial direction to decrease the readout time.

Data reduction was undertaken using optimal extraction (Horne 1986) as implemented in the PAMELA[3] code (Marsh 1989), which also makes use of the STARLINK[4] packages FIGARO and KAPPA. Telluric lines removal and flux-calibration was performed separately for each night, using observations of flux standard stars.

Wavelength calibrations were obtained in a standard fashion using spectra of copper–argon and copper–neon arc lamps. For SDSS 0303, arc lamp exposures were obtained during the spectroscopic observations and the wavelength solutions were interpolated from the two arc spectra bracketing each spectrum. For the other objects we did not obtain dedicated arc spectra to increase the time efficiency of the observations. The spectra were wavelength calibrated using arc exposures taken at the beginning of each night, and drift in the wavelength solution was removed using measurements of the positions of the λ7913 and λ6300 night-sky emission lines. This procedure has been found to work well for spectra at red wavelengths (see Southworth et al. 2006; Southworth et al. 2008). In the blue arm, a reliable correction of the wavelength zero-point was not possible as only one (moreover weak) sky-line (Hg I λ4358) is available, and consequently, these spectra are not suitable for velocity measurements. The reciprocal dispersion and resolution for the R316R grating are approximately 1.7 Å pixel^{-1} and 3.3 Å, and for the R600R grating are 0.89 Å pixel^{-1} and 1.5 Å, respectively.

[2] IRAF is distributed by the National Optical Astronomy Observatory, which is operated by the Association of Universities for Research in Astronomy, Inc., under contract with the National Science Foundation, http://iraf.noao.edu

[3] PAMELA and MOLLY were written by TRM and can be found at http://www.warwick.ac.uk/go/trmarsh

[4] The STARLINK software can be found at http://starlink.jach.hawaii.edu/

4 ORBITAL PERIODS AND EPHEMERIDES

Mid-eclipse times for all four systems were measured from their light curves as follows. The observed eclipse profile was mirrored in time around an estimate of the eclipse centre. The mirrored profile was then overplotted on the original eclipse profile and shifted against it, until the best overlap between the points during ingress and egress was found. Given the sharpness of eclipse in/egress features, we (conservatively) estimate the error in the mid-eclipse times to be comparable to the duty cycle (exposure plus readout time) of the observations. Table 3 lists the mid-eclipse times. An initial estimate of the cycle count was then obtained by fitting eclipse phases $(\phi_0^{\rm observed} - \phi_0^{\rm fit})^{-2}$ over a wide range of trial periods. Once an unambiguous cycle count was established, a linear eclipse ephemeris was fitted to the times of mid-eclipse. For SDSS 1435+3733 we have also used the mid-eclipse times provided by Steinfadt et al. (2008). The resulting ephemerides, with numbers in parenthesis indicating the error on the last digit, are

$$T_0({\rm HJD}) = 245\,3994.44787(9) + 0.3326\,873(1)E \quad (1)$$

for SDSS 0110+1326, that is, $P_{\rm orb} = 7.984\,495(3)$ h,

$$T_0({\rm HJD}) = 245\,3991.6164(1) + 0.13\,443\,772(7)E \quad (2)$$

for SDSS 0303+0054, that is, $P_{\rm orb} = 3.226\,505(1)$ h,

$$T_0({\rm HJD}) = 245\,4148.70\,361(6) + 0.1256\,311(1)E \quad (3)$$

for SDSS 1435+3733, that is, $P_{\rm orb} = 3.015\,144(2)$ h and

$$T_0({\rm HJD}) = 245\,4592.57\,135(6) + 0.18\,551\,774(4)E \quad (4)$$

for SDSS 1548+4057, that is, $P_{\rm orb} = 4.45\,242\,576(4)$ h.

These ephemerides were then used to fold both the photometric and the spectroscopic data over phase (Fig. 1).

5 RADIAL VELOCITIES OF THE SECONDARY STARS

Fig. 2 shows the SDSS spectra of our four targets. Measuring radial velocity variations of the stellar components needs sharp spectral features. Determining the radial velocity amplitude of the white dwarf, $K_{\rm WD}$, is notoriously difficult because of the width of the Balmer lines, and our spectroscopic data are insufficient in quantity and signal-to-noise ratio for the approach outlined e.g. by Maxted et al. (2004).[5] We hence restrict our analysis to the measurement of the radial velocity amplitude of the secondary star, $K_{\rm sec}$.

5.1 SDSS 0110+1326

The spectrum of SDSS 0110+1326 displays the Ca II λλ8498.02, 8542.09, 8662.14 emission triplet as well as an Hα emission line. We determined the velocities of the Hα emission line by fitting a second-order polynomial plus a Gaussian emission line to the spectra. For the Ca II triplet, we fitted a second-order polynomial plus three Gaussian emission lines with identical width and whose separations were fixed to the corresponding laboratory values (see Fig. 3, right-hand panel). The Hα and Ca II radial velocities were then separately phase folded using the ephemeris equation (1), and

[5] Ultraviolet spectroscopy allows accurate measurements of $K_{\rm WD}$ using narrow metal lines originating in the white dwarf photosphere (O'Brien, Bond & Sion 2001; O'Donoghue et al. 2003; Kawka et al. 2007), but at the cost of space-based observations.

Table 3. Mid-eclipse timings, cycle number and the difference between observed and computed eclipse times using the ephemerides provided in equations (1)–(4). The large O − C values for the first five eclipses of SDSS 1548+4057 are due to the poor time resolution of the IAC 80 light curves (Table 2). Mid-eclipse times for SDSS 1435+3733 from Steinfadt et al. (2008) are also included.

System	T_0 (HJD)	Cycle	O − C (s)	System	T_0 (HJD)	Cycle	O − C (s)
SDSS 0110+1326	245 3994.447 919	0	+4		245 4150.71 397	16	+22
	245 3995.445 757	3	−16		245 4239.40 916	722	−6
	245 3996.444 139	6	+12		245 4240.41 415	730	−10
	245 4383.692 048	1170	0		245 4240.66 553	732	−1
SDSS 0303+0054	245 3991.616 630	0	+20		245 4249.71 103	804	+5
	245 3993.498 445	14	−1		245 4251.72 113	820	+6
	245 3994.708 508	23	−2		245 4252.85 179	829	+4
	245 3997.531 505	44	−12	**SDSS 1548+4057**	245 4592.57 222	0	71
	245 4339.675 049	2559	−12		245 4597.39 591	26	92
	245 4335.642 243	2589	−26		245 4597.57 771	27	−230
	245 4389.55 246	2960	+33		245 4599.62 180	38	185
SDSS 1435+3733	245 4148.70 346	0	−13		245 4644.51 613	280	−11
	245 4149.70 865	8	−1		245 4647.48 471	296	15
	245 4150.58 802	15	−5		245 4653.42 122	328	11

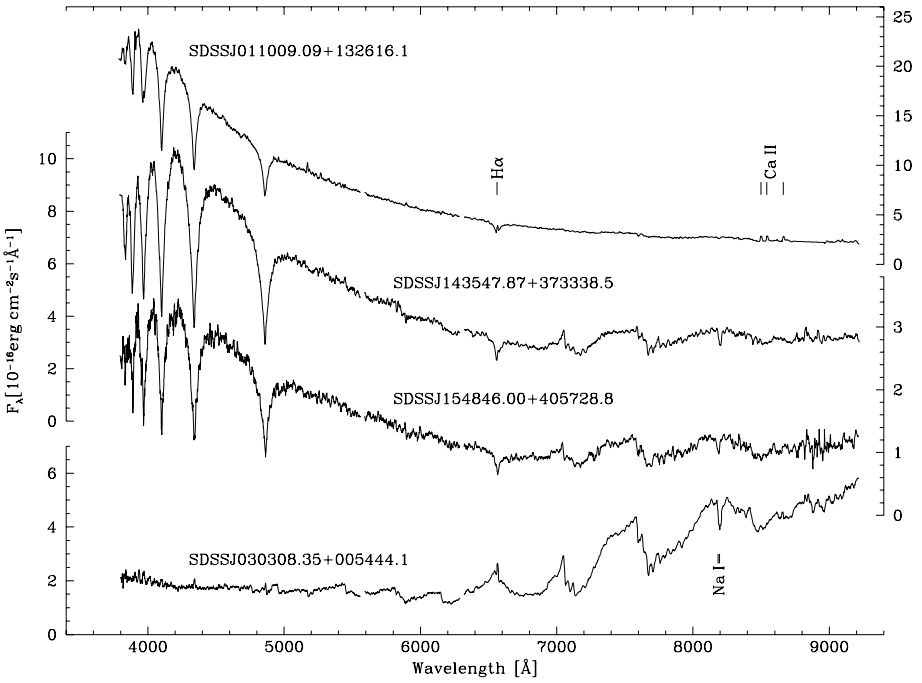

Figure 2. SDSS spectra of the four systems. Top to bottom: SDSS 0110+ 1326, SDSS 1435+3733 SDSS 1548+4057 and SDSS 0303+0054. The radial velocity of the companion star in SDSS 0110+1326 was measured from the H α and Ca II emission lines, whereas for the other three systems, we used the Na I absorption doublet.

fitted with a sine wave. The phasing of the radial velocity curves agreed with that expected from an eclipsing binary (i.e. red-to-blue crossing at orbital phase zero) within the errors. The resulting radial velocity amplitudes are $K_{\rm sec,\,H\alpha} = 200.1 \pm 4.8\,{\rm km\,s^{-1}}$ with a systemic velocity of $\gamma_{\rm H\alpha} = 19.4 \pm 4.1\,{\rm km\,s^{-1}}$ for the H α line; and $K_{\rm sec,Ca\,II} = 178.8 \pm 2.4\,{\rm km\,s^{-1}}$ and $\gamma_{\rm Ca\,II} = 15.2 \pm 2.4\,{\rm km\,s^{-1}}$ for the Ca II line (see also Fig. 1).

We decided, following a suggestion by the referee, to investigate whether the emission lines originate predominantly on the illuminated hemisphere of the secondary star. If that is the case – keeping in mind that we see the system almost edge-on – we expect a significant variation of the line strength with orbital phase, reaching a maximum around phase $\phi = 0.5$ (superior conjunction of the secondary) and almost disappearing around $\phi = 0.0$. Fig. 4 shows average spectra of SDSS 0110+1326, focused on the Hα line and the Ca II triplet for $\phi = 0.0$ and 0.5. It is apparent that the Hα and Ca II emission lines are very strong near $\phi = 0.5$. The Hα emission line is very weak near $\phi = 0.0$, and Ca II is seen in absorption. The equivalent width (EW) of the blue-most component of the Ca II triplet is shown in Fig. 5 (top panel) as a function of orbital phase. Given the spectral resolution and quality of our data, measuring the EW of the Hα emission line is prone to substantial uncertainties, as it is embedded in the broad Hα absorption of the white dwarf photosphere (see Fig. 2 again), but it generally follows a similar pattern as the one seen in the Ca II triplet. This analysis supports our assumption that the emission lines originate on the irradiated, inner

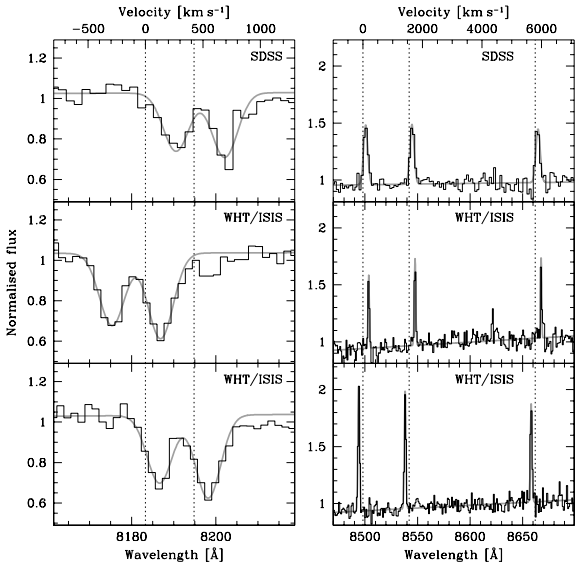

Figure 3. Sample line profile fits (grey) to the observed spectra (black) of SDSS 0303+0054 (left-hand panel, Na I λλ8183.27, 8194.81 absorption doublet) and of SDSS 0110+1326 (right-hand panel, Ca II emission triplet). The rest wavelengths are indicated by the dotted vertical lines. The velocity scale at the top is relative to the blue-most component of each multiplet. The top spectra are from SDSS, the middle and bottom spectra were obtained at the WHT. Radial velocity variations in these systems are obvious to the eye.

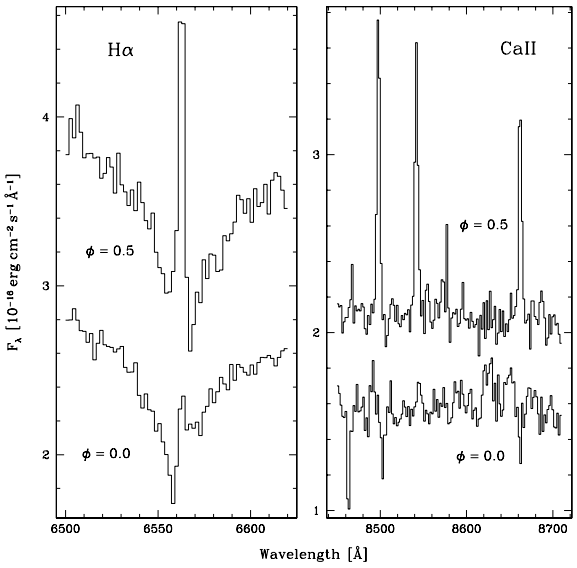

Figure 4. Average spectra of SDSS 0110+1326. Left-hand panel: Hα line; right-hand panel: Ca II triplet. The binary phase of each spectrum is clearly marked. Prior to averaging, each spectrum was shifted to the rest frame of the secondary, using the measured $K_{\rm sec}$ and γ values. For each line and binary phase, three spectra were averaged.

hemisphere of the secondary star. Hence, the centre of light of the secondary star is displaced towards the Lagrangian point L_1, with respect to the centre of mass. The emission lines trace, therefore, the movement of the centre of light and not the centre of mass and as a result, the $K_{\rm sec}$ values measured from either the Hα or the Ca II emission lines are very unlikely to represent the true radial velocity amplitude of the secondary star, but instead give a lower limit to it.

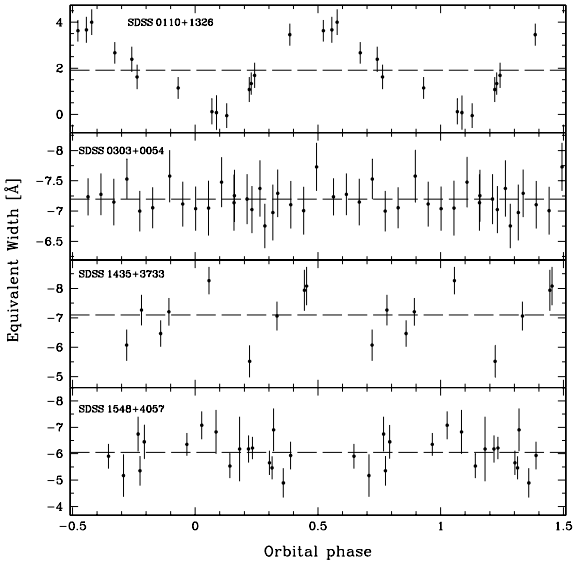

Figure 5. EWs of the lines used to measure radial velocities in all four systems with respect to the orbital phase. Top panel: blue-most component of the Ca II emission triplet in SDSS 0110+1326. Lower three panels: blue-most component of the Na I absorption doublet in SDSS 0303+0054, SDSS 1435+3733 and SDSS 1548+4057, respectively. The dashed lines indicate the mean EW. The strong variation of the EW of the Ca II emission line is obvious. No significant variation as a function of phase is observed for the other three systems. A full orbital cycle has been duplicated for clarity.

The fact that $K_{\rm sec}$ measured from the H α line is larger than that from the Ca II line suggests that the H α emission is distributed in a slightly more homogeneous fashion on the secondary, and illustrates that correcting the observed $K_{\rm sec}$ for the effect of irradiation is not a trivial matter. We describe our approach to this issue in Section 8.2.

5.2 SDSS 0303+0054, SDSS 1435+3733 and SDSS 1548+4057

The Na I λλ8183.27, 8194.81 absorption doublet is a strong feature in the spectra of SDSS 0303+0054, SDSS 1435+3733 and SDSS 1548+4057. We measured the radial velocity variation of the secondary star in SDSS 0303+0054 by fitting this doublet with a second-order polynomial plus two Gaussian emission lines of common width and a separation fixed to the corresponding laboratory value (see Fig. 3, left-hand panel). The same method was applied to the spectra of SDSS 1435+3733 and SDSS 1548+4057. A sine-fit to each of the radial velocities data sets, phase folded using the ephemerides equations (2)–(4), gives the radial velocity of the secondary star, $K_{\rm sec}$, and the systemic velocity γ for each system. The results of the radial velocity measurements are summarized in Table 4.

No significant variation in the strength of the Na I doublet was observed as a function of orbital phase, and we hence assume

Table 4. Summary of the radial velocity measurements for all four systems.

System	Line	$K_{\rm sec}$ (km s^{-1})	γ (km s^{-1})
SDSS 0110+1326	Hα	200.1 ± 4.8	19.4 ± 4.1
	Ca II	178.8 ± 2.4	15.2 ± 2.4
SDSS 0303+0054	Na I	339.7 ± 1.9	-4.0 ± 1.4
SDSS 1435+3733	Na I	260.9 ± 2.9	47.4 ± 2.2
SDSS 1548+4057	Na I	274.7 ± 2.6	-7.4 ± 2.2

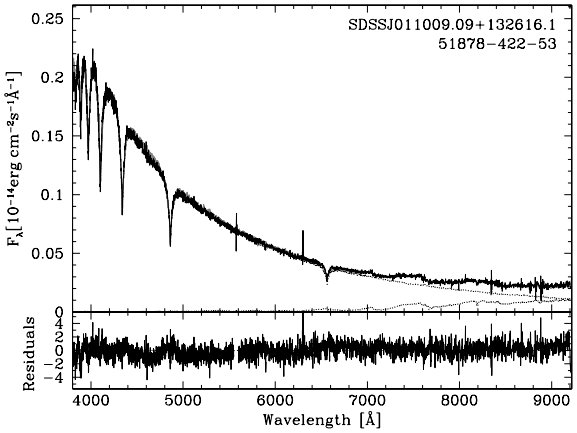

Figure 6. Two-component fit to the spectrum of SDSS 0110+1326. The top panel shows the spectrum of the object as a solid black line and the two templates, white dwarf and M dwarf, as dotted lines. The bottom panel shows the residuals from the fit.

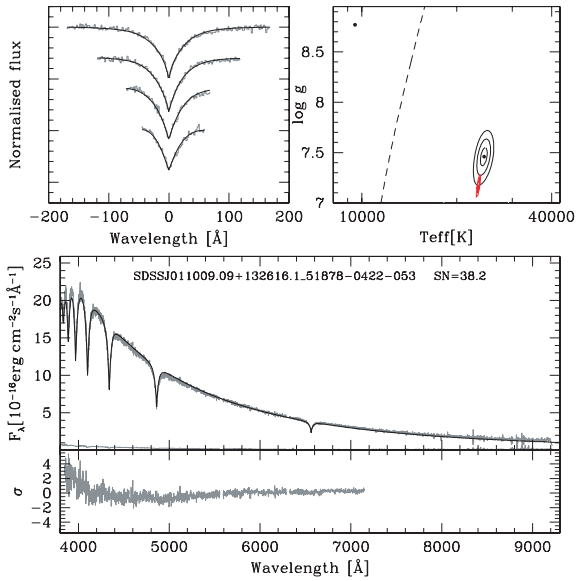

Figure 7. Spectral model fit to the white dwarf in SDSS 0110+1326, obtained after subtracting the best-fitting M-dwarf template. Top left-hand panel: best fit (black lines) to the observed Hβ to Hϵ (grey lines, top to bottom) line profiles. The model spectra and observations have been normalized in the same way. Top right-hand panel: 1, 2 and 3σ contour plots in the $T_{\rm eff}$–log g plane. The black contours refer to the best line profile fit, the red ones (which collapse into a dot on the scale of the plot) to the fit of the spectral range 3850–7150 Å. The dashed line indicates the occurrence of maximum Hβ EW. The best 'hot' and 'cold' line profile solutions are indicated by black dots, while the best fit to the whole spectrum by a red one. Bottom panel: the residual white dwarf spectrum resulting from the spectral decomposition and their flux errors (grey lines) along with the best-fitting white dwarf model (black line) in the 3850–7150 Å wavelength range (top) and the residuals of the fit (grey line, bottom).

that $K_{\rm sec}$ measured from this doublet reflects the true radial velocity amplitudes of the secondary stars in SDSS 0303+0054, SDSS 1435+3733 and SDSS 1548+4057. This is illustrated in Fig. 5, where we plot the EWs against orbital phase for these three systems.

6 SPECTROSCOPIC STELLAR PARAMETERS

We used the spectral decomposition/fitting method described in detail in Rebassa-Mansergas et al. (2007) to estimate the white dwarf effective temperatures ($T_{\rm eff}$) and surface gravities (log g), as well as the spectral types of the companion stars, for our four targets from their SDSS spectroscopy.

Briefly, the method employed is the following: as a first step a two-component model is fitted to the WDMS binary spectrum using a grid of observed M dwarf and white dwarf templates. This step determines the spectral type and flux contribution of the M-dwarf component as shown in Fig. 6. After subtracting the best-fitting M dwarf, the residual white dwarf spectrum is fitted with a grid of white dwarf model spectra from Koester et al. (2005). We fit the normalized Hβ to Hϵ line profiles, omitting Hα which is most severely contaminated by the continuum and/or Hα emission from the companion star. Balmer line profile fits can lead to degeneracy in the determination of $T_{\rm eff}$ and log g, as their EWs go through a maximum at $T_{\rm eff} \simeq 13000$ K, which means that fits of similar quality can be achieved for a 'hot' and 'cold' solution. In order to select the physically correct solution, we also fit the continuum plus Balmer lines over the range 3850–7150 Å. The resulting $T_{\rm eff}$ and log g are less accurate than those from line profile fits, but sensitive to the slope of the spectrum, and hence allow in most cases to break the degeneracy between the hot and cold solutions. Fig. 7 illustrates this procedure. Once $T_{\rm eff}$ and log g are determined, the white dwarf mass and radius can be estimated using an updated version of Bergeron, Wesemael & Beauchamp's (1995) tables. The results, after applying this method to our four systems, are summarized in Table 5. The preferred solution ('hot' or 'cold') is highlighted in bold font.

In the case of SDSS 0303+0054, which contains a DC white dwarf (Fig. 2), the spectral decomposition results in Sp(2) = M 4.5 ± 0.5 for the secondary star. The subsequent fit to the residual white dwarf spectrum is not physical meaningful, as the white dwarf in SDSS 0303+0054 does not exhibit Balmer lines. The fit to the overall spectrum, which is purely sensitive to the continuum slope, suggests $T_{\rm eff} < 8000$ K, which is consistent with the DC classification of the white dwarf.

Table 5. Summary of the results obtained for SDSS 0110+1326, SDSS 1435+3733 and SDSS 1548+4057 from our spectral decomposition technique. The preferred set of parameters for each system is highlighted in bold font.

Solution	$M_{\rm WD}$ ($M_\odot$)	log g	$T_{\rm eff}$ (K)	Sp (2)
SDSS 0110+1326				
Hot	**0.47 ± 0.02**	**7.65 ± 0.05**	**25891 ± 427**	**M4 ± 1**
Cold	1.2 ± 0.03	9 ± 0.04	9619 ± 23	M 4 ± 1
SDSS 1435+3733				
Hot	0.40 ± 0.05	7.58 ± 0.11	12536 ± 438	M 4.5 ± 0.5
Cold	**0.41 ± 0.05**	**7.62 ± 0.12**	**12536 ± 488**	**M4.5 ± 0.5**
SDSS 1548+4057				
Hot	0.43 ± 0.16	7.64 ± 0.31	14899 ± 1300	M 6 ± 0.5
Cold	**0.62 ± 0.28**	**8.02 ± 0.44**	**11699 ± 820**	**M6 ± 0.5**

7 BASIC EQUATIONS

Here, we introduce the set of equations that we will use to constrain the stellar parameters of our four eclipsing WDMS binaries. In a binary system, where a white dwarf primary and a main-sequence

companion, with masses $M_{\rm WD}$ and $M_{\rm sec}$, respectively, orbit with a period $P_{\rm orb}$ around their common centre of mass at a separation $a = a_{\rm WD} + a_{\rm sec}$ where $a_{\rm WD}\,M_{\rm WD} = a_{\rm sec}\,M_{\rm sec}$, the orbital velocity K of either star, as observed at an inclination angle i, is

$$K_j = \frac{2\pi a_j}{P_{\rm orb}} \sin i \qquad j = {\rm WD, sec}, \tag{5}$$

assuming circular orbits. Given Kepler's law

$$a^3 = \frac{G\,(M_{\rm WD} + M_{\rm sec})\,P_{\rm orb}^2}{4\pi^2} \tag{6}$$

and using

$$a = a_{\rm WD}\frac{M_{\rm WD} + M_{\rm sec}}{M_{\rm sec}} \tag{7}$$

one can obtain the two mass functions:

$$f\,(M_{\rm sec}) = \frac{(M_{\rm sec}\sin i)^3}{(M_{\rm WD} + M_{\rm sec})^2} = \frac{P_{\rm orb}K_{\rm WD}^3}{2\pi G} < M_{\rm sec}, \tag{8}$$

$$f\,(M_{\rm WD}) = \frac{(M_{\rm WD}\sin i)^3}{(M_{\rm WD} + M_{\rm sec})^2} = \frac{P_{\rm orb}K_{\rm sec}^3}{2\pi G} < M_{\rm WD} \tag{9}$$

which give strict lower limits on the masses of the components. From these two equations we get

$$q = \frac{M_{\rm sec}}{M_{\rm WD}} = \frac{K_{\rm WD}}{K_{\rm sec}}. \tag{10}$$

Therefore, the knowledge of the radial velocities of both stars can immediately yield the mass ratio q of the system, using equation (10). In our case, since we lack a measurement for the radial velocity of the white dwarf $K_{\rm WD}$, a more indirect approach needs to be followed. Re-arranging equation (9) for $\sin i$ yields

$$\sin i = \left[\frac{P_{\rm orb}K_{\rm sec}^3}{2\pi G}\frac{(M_{\rm WD} + M_{\rm sec})^2}{M_{\rm WD}^3}\right]^{1/3}, \tag{11}$$

whereas re-arranging equation (9) for $K_{\rm sec}$ yields

$$K_{\rm sec} = \left[\frac{2\pi G\sin^3 i}{P_{\rm orb}}\frac{M_{\rm WD}^3}{(M_{\rm WD} + M_{\rm sec})^2}\right]^{1/3}. \tag{12}$$

We make use of equations (11) and (12) in the light-curve fitting process described in the next section.

For the DC white dwarf in SDSS 0303+0054, where we lack a spectroscopic estimate of $M_{\rm WD}$, we can use equation (9) to get a rough, first estimate of the white dwarf mass. In Fig. 8, we have plotted equation (9) for $i = 90^\circ$ and 78°. For lower inclinations no eclipses occur for $K_{\rm sec} = 339.7\,{\rm km\,s^{-1}}$ and $P_{\rm orb} = 0.134\,{\rm d}$. For a given choice of the inclination angle, equation (9) defines a unique relation $M_{\rm sec}(M_{\rm WD})$. If we further assume a mass for the secondary, we can investigate the possible range of the white dwarf mass for SDSS 0303+0054. For an extremely conservative lower limit of $M_{\rm sec} \geq 0.08\,{\rm M}_\odot$ (the lower mass limit for an M dwarf, e.g. Dorman, Nelson & Chau 1989, with the spectrum of SDSS 0303+0054 clearly identifying the companion as a main-sequence star), $M_{\rm WD} \geq 0.68\,{\rm M}_\odot$. Even under this extreme assumption for the companion star, the white dwarf in SDSS 0303+0054 has to be more massive than the average field white dwarf (Koester, Schulz & Weidemann 1979; Liebert, Bergeron & Holberg 2005). If we assume Sp (2) = M 4, the upper limit of the spectral type according to our spectral decomposition of the SDSS spectrum, and use the spectral type–mass relation of Rebassa-Mansergas et al. (2007), we find $M_{\rm sec} \simeq 0.32\,{\rm M}_\odot$, and hence $M_{\rm WD} \geq 0.96\,{\rm M}_\odot$. These estimates assume $i = 90^\circ$, for lower inclinations the respective $M_{\rm WD}$ values become larger, as illustrated in Fig. 8. In summary, based on $K_{\rm sec}$, $P_{\rm orb}$ and a generous range in possible $M_{\rm sec}$ we expect the white dwarf in SDSS 0303+0054 to be fairly massive, $0.7 \lesssim M_{\rm WD} \lesssim 1.0\,{\rm M}_\odot$.

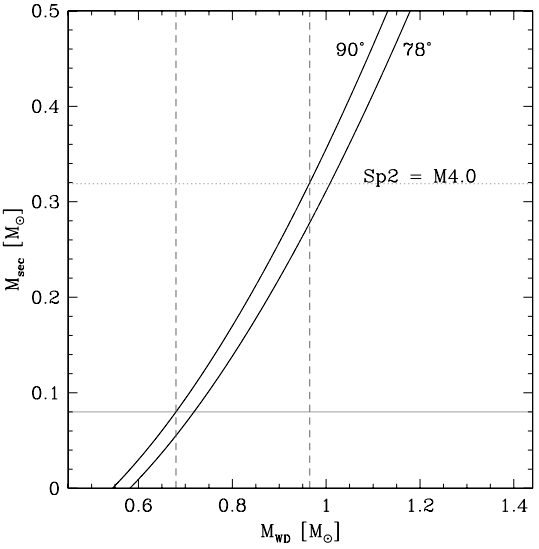

Figure 8. Mass function plot (see equation 9) for SDSS 0303+0054, for $i = 78^\circ$ and 90°. The grey horizontal line corresponds to a lower mass limit for M dwarfs. The dotted horizontal line is the value of $M_{\rm sec}$, corresponding to a secondary spectral type of Sp (2) = M 4, assuming a Sp (2)–$M_{\rm sec}$ relation. The dashed vertical lines indicate the corresponding range for the white dwarf mass.

8 LIGHT-CURVE MODEL FITTING

Analysing the light curves of eclipsing binaries can provide strong constraints on the physical parameters of both stars. Here, we make use of a newly developed code written by one of us (TRM) for the general case of binaries containing a white dwarf. The code offers the option to include accretion components (disc, bright spot) for the analysis of cataclysmic variables (CVs) – given the detached nature of our targets, those components were not included. The program subdivides each star into small elements with a geometry fixed by its radius as measured along the direction of centres towards the other star. The code allows for the distortion of Roche geometry and for irradiation of the main-sequence star using the approximation $\sigma T_{\rm sec}'^4 = \sigma T_{\rm sec}^4 + F_{\rm irr}$, where $T'_{\rm sec}$ is the modified temperature and $T_{\rm sec}$ the temperature of the unirradiated companion, σ is the Stefan–Boltzmann constant and $F_{\rm irr}$ is the irradiating flux, accounting for the angle of incidence and distance from the white dwarf. The white dwarf is treated as a point source in this calculation and no backwarming of the white dwarf is included. The latter is invariably negligible, while the former is an unnecessary refinement given the approximation inherent in treating the irradiation in this simple manner.

The code computes a model based on input system parameters supplied by the user. Starting from this parameter set, model light curves are then fitted to the data using Levenberg–Marquardt minimization, where the user has full flexibility as to which parameters will be optimized by the fit, and which ones will be kept fixed at the initial value.

The physical parameters, which define the models, are the radii scaled by the binary separation, $R_{\rm WD}/a$ and $R_{\rm sec}/a$, the orbital inclination, i, the unirradiated stellar temperatures of the white dwarf and the secondary star $T_{\rm eff,WD}$ and $T_{\rm eff,sec}$, respectively, the mass ratio $q = M_{\rm sec}/M_{\rm WD}$, T_0 the time of mid-eclipse of the white dwarf and d the distance. We account for the distance simply as a scaling factor that can be calculated very rapidly for any given model, and so it does not enter the Levenberg–Marquardt optimization. All other

parameters can be adjusted, i.e. be allowed to vary during the fit, but typically the light curve of a given system does not contain enough information to constrain all of them simultaneously. For instance, for systems with negligible irradiation, fitting $T_{\rm eff,WD}, T_{\rm eff,sec}$ and d simultaneously is degenerate since a change in distance can be exactly compensated by changes in the temperatures.

Some of our exposures were of a significant length compared to the length of the white dwarf's ingress and egress and therefore we subdivided the exposures during the model calculation, trapezoidally averaging to obtain the estimated flux.

Our aim is to combine the information from the $K_{\rm sec}$ radial velocity amplitudes determined in Section 5, the information contained in the light curve and the white dwarf effective temperature determined from the spectral fit in Section 6 to establish a full set of stellar parameters for the four eclipsing WDMS binaries. The adopted method is described in the next two subsections, where SDSS 0110+1326 requires a slightly broader approach, as a correction needs to be applied to the $K_{\rm sec}$ velocity determined from the emission lines.

8.1 SDSS 0303+0054, SDSS 1435+3733 and SDSS 1548+4057

Our approach is to fit a light-curve model to the data for a selected grid of points in the $M_{\rm WD}$–$M_{\rm sec}$ plane. Each point in the $M_{\rm WD}$–$M_{\rm sec}$ plane defines a mass ratio q (equation 10), and, using $K_{\rm sec}$ and $P_{\rm orb}$, a binary inclination i (equation 11). Hence, a light-curve fit for a given $(M_{\rm WD}, M_{\rm sec})$ combination will have $M_{\rm WD}, M_{\rm sec}, q$ and i fixed, whereas $R_{\rm WD}, R_{\rm sec}, T_{\rm eff,sec}, T_{\rm eff,WD}$ and T_0 are in principle free parameters. In practice, we fix $T_{\rm eff,WD}$ to the value determined from the spectroscopic fit, which is sufficiently accurate, hence only $R_{\rm WD}, R_{\rm sec}, T_{\rm eff,sec}$ and T_0 are free parameters in the light-curve fits. We leave T_0 free to vary to account for the O-C errors in each individual light curve. The fitted values of T_0 were of the order of 10 s, consistent with the O-C values quoted in Table 3. Each light-curve fit in the $M_{\rm WD}$–$M_{\rm sec}$ plane requires some initial estimates of $R_{\rm WD}, R_{\rm sec}, T_{\rm eff,sec}$. For $R_{\rm WD}$ we adopt the theoretical white dwarf mass–radius relation interpolated from Bergeron et al.'s (1995) tables. For $R_{\rm sec}$ we use the mass–radius relation of Baraffe et al. (1998), adopting an age of 5 Gyr. For $T_{\rm eff,sec}$, we use the spectral type of the secondary star as determined from the spectral decomposition (Section 6) combined with the spectral type–temperature relation from Rebassa-Mansergas et al. (2007). $R_{\rm WD}$ and $R_{\rm sec}$ are then scaled by the binary separation, equation (7).

We defined large and densely covered grids of points in the $M_{\rm WD}$–$M_{\rm sec}$ plane which generously bracket the initial estimates for $M_{\rm WD}$ and $M_{\rm sec}$ based on the spectral decomposition/fitting. For SDSS 0303+0054, where no spectral fit to the white dwarf is available, we bracket the range in $M_{\rm WD}$ illustrated in Fig. 8. Points for which (formally) $\sin i > 1$ were discarded from the grid, for all other points a light-curve fit was carried out, recording the resulting $R_{\rm WD}, R_{\rm sec}$ and $T_{\rm eff,sec}$. The number of light-curve fits performed for each system was between 7000 and 10 000, depending on the system.

8.2 SDSS 0110+1326

In the case of SDSS 0110+1326 the inclination angle cannot readily be calculated through equation (11), as we measured $K_{\rm sec}$ from either the Hα or Ca II emission lines, which do not trace the motion of the secondary's centre of mass, but the centre of light in the given emission line. The general approach in this case is to apply a correction to the observed $K_{\rm sec}$, where the motion of the secondary star's centre of mass, $K_{\rm sec,\,cor}$ is expressed according to Wade & Horne (1988) as

$$K_{\rm sec,\,cor} = \frac{K_{\rm sec}}{1-(1+q)(\Delta R/a)}, \tag{13}$$

where $K_{\rm sec}$ is the measured radial velocity, q is the mass ratio of the system, a the binary separation and ΔR is the displacement of the centre of light from the centre of mass of the secondary. ΔR can have a minimum value of zero, i.e. the two centres coincide and no correction is needed and a maximum value of $R_{\rm sec}$, i.e. all light comes from a small region of the secondary star closest to the primary. An assumption often used in the literature is that the emission due to irradiation is distributed uniformly over the inner hemisphere of the secondary star, and is zero on its unirradiated side, in which case $\Delta R = (4/3\pi)\, R_{\rm sec}$ (e.g. Wade & Horne 1988; Wood, Robinson & Zhang 1995b; Orosz et al. 1999; Vennes, Thorstensen & Polomski 1999). A more physical model of the distribution of the irradiation-induced emission-line flux can be derived from the analysis of the orbital variation of the EW of the emission line. A fine example of this approach is the detailed study of the Ca II $\lambda\lambda$8498.02, 8542.09, 8662.14 emission in the WDMS binary HR Cam presented by Maxted et al. (1998). However, given the small number of spectra, it is currently not possible to apply this method to SDSS 0110+1326.

Our approach for modelling SDSS 0110+1326 was to calculate the binary separation from equation (6) for each pair of ($M_{\rm WD}$, $M_{\rm sec}$) of the initial grid and then, using equation (13), calculate various possible $K_{\rm sec,\,cor}$ values for this ($M_{\rm WD}$, $M_{\rm sec}$) point, assuming various forms of ΔR. We adopted the following three different cases: (i) $\Delta R = 0$, i.e. the centre of light coincides with the centre of mass, (ii) $\Delta R = (4/3\pi)R_{\rm sec}$, i.e. the uniform distribution case and (iii) $\Delta R = R_{\rm sec}$, i.e. the maximum possible displacement of the centre of light. This was done for both the H α and the Ca II lines. Having attributed a set of corrected radial velocity values to each point of the grid, we could now make use of equation (11) to calculate the corresponding inclination angles. Again, points with a (formal) $\sin i > 1$ were eliminated from the grid. The allowed ($M_{\rm WD}$, $M_{\rm sec}$) pairs for both lines and all three ΔR cases are shown in Fig. 9.

The first of the three ΔR cases, $\Delta R = 0$, is obviously not a physically correct approach, as it implies that no correction is necessary. However, we did use it as a strict lower limit of the radial velocity of the secondary. In this sense, the third case, $\Delta R = R_{\rm sec}$, is a strict upper limit for $K_{\rm sec}$. Table 6 lists the ranges $K_{\rm sec,cor}$ corresponding the our adopted grid in the ($M_{\rm WD}$, $M_{\rm sec}$) plane shown in Fig. 9.

9 RESULTS

Our light-curve fitting procedure outlined in Section 8 yields fitted values for $R_{\rm WD}, R_{\rm sec}$ and $T_{\rm eff,sec}$ for a large grid in the $M_{\rm WD}$–$M_{\rm sec}$ plane, where each ($M_{\rm WD}$, $M_{\rm sec}$) point defines q and i. Analysing these results was done in the following fashion.

In a first step, we applied a cut in the quality of the light-curve fits, where we considered three different degrees of 'strictness' by culling all models whose χ^2 was more than 1, 2 or 3σ above the best-fitting value. This typically left us with a relatively large degeneracy in $M_{\rm WD}$ and $M_{\rm sec}$.

In a second step, we had to select among various equally good light-curve fits those that are physically plausible. Given that our set of fitted parameters was underconstrained by the number of observables, we had to seek input from theory in the form of mass–radius relations for the white dwarf (using the tables of Bergeron et al. 1995) and for the M dwarf (using the 5.0 Gyr model of Baraffe

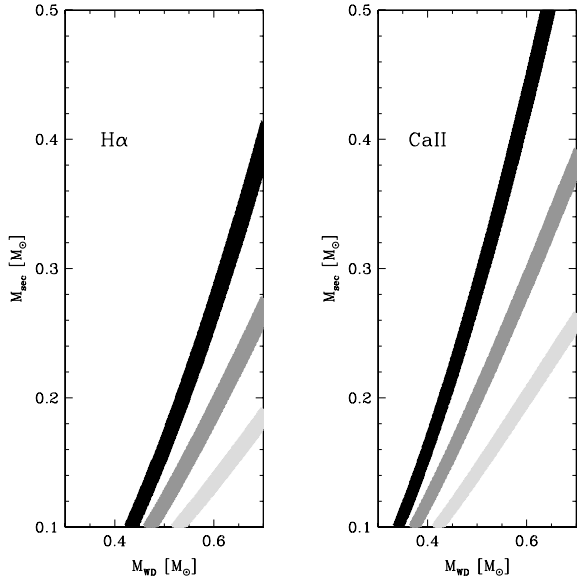

Figure 9. Grid of ($M_{\rm WD}$, $M_{\rm sec}$) points for which the light curve of SDSS 0110+1326 has been fitted. Different assumptions for the *K*-correction were made: $\Delta R = 0$ (black strip), $\Delta R = (4/3\pi)R_{\rm sec}$ (dark grey strip) and $\Delta R = R_{\rm sec}$ (light grey strip). Left-hand panel: ($M_{\rm WD}$, $M_{\rm sec}$) grid for $K_{\rm sec} = K_{\rm sec,\,H\alpha} = 200.1\,{\rm km\,s^{-1}}$. Right-hand panel: ($M_{\rm WD}$, $M_{\rm sec}$) grid for $K_{\rm sec} = K_{\rm sec,\,Ca\,II} = 178.8\,{\rm km\,s^{-1}}$.

Table 6. Corrected values of the radial velocity of the secondary star in SDSS 0110+1326, after assuming a form of ΔR, for both the cases of the H α and the Ca II emission lines.

ΔR	Mean (km s^{-1})	Std. dev.	Range (km s^{-1})
Hα			
0	200.1	–	–
$(4/3\pi)R_{\rm sec}$	213.1	2.7	207.9–218.2
$R_{\rm sec}$	225.2	3.5	218.5–232.1
Ca II			
0	178.8	–	–
$(4/3\pi)R_{\rm sec}$	195.1	4.2	186.6–202.7
$R_{\rm sec}$	209.1	6.1	197.2–219.9

et al. 1998). We then calculated for each model the relative difference between the theoretical value of the radius and the value of the radius from the fit:

$$\delta R = \left| \frac{R_{\rm fit} - R_{\rm th}}{R_{\rm th}} \right|, \qquad (14)$$

where $R_{\rm fit}$ and $R_{\rm th}$ are the radius obtained from the light-curve fit, and the radius from the mass–radius relation, respectively. Assuming that the binary components obey, at least to some extent, a theoretical mass–radius relation, we defined cut-off values of $\delta R = 5$, 10 and 15 per cent, above which light-curve models will be culled. The maximum of $\delta R = 15$ per cent was motivated by the radius excess over theoretical main-sequence models observed in eclipsing low-mass binaries (Ribas et al. 2008), and by the current observational constraints on the white dwarf mass–radius relation (Provencal et al. 1998). This cut in radius was applied individually for the white dwarf ($\delta R_{\rm WD}$) and the companion star ($\delta R_{\rm sec}$).

Combining both the χ^2 and δR cuts left us in general with a relatively narrow range of system parameters that simultaneously satisfy the radial velocity amplitude and the morphology of the light curve. In a final step, we examined how well the stellar masses determined from the light curve/radial velocity analysis agreed with those derived from the spectral decomposition.

9.1 SDSS 0303+0054

Modelling the light curve of SDSS 0303+0054 involved the following two problems. First, the time resolution of our data set poorly resolves the white dwarf ingress and egress phases, and consequently the white dwarf radius can only be loosely constrained. We decided therefore to fix the white dwarf radius in the light-curve fits to the value calculated from the adopted white dwarf mass–radius relation of Bergeron et al. (1995). Secondly, the light curve displays a strong, but slightly asymmetric ellipsoidal modulation, with the two maxima being of unequal brightness (Fig. 1). Similar light-curve morphologies have been observed in the WDMS binaries BPM 71214 (Kawka & Vennes 2003) and LTT 560 (Tappert et al. 2007), and have been attributed to star-spots on the secondary star. By design, our light-curve model can not provide a fit that reproduces the observed asymmetry. Having said this, the presence of ellipsoidal modulation provides an additional constraint on $R_{\rm sec}$ that is exploited by the light-curve fit.

A number of models passed the strictest configuration of our cut-offs, i.e. 1σ and $\delta R_{\rm sec} = 5$ per cent (no cut was used in $\delta R_{\rm WD}$, as $R_{\rm WD}$ has been fixed during the fits). The possible range of solutions in the $M_{\rm WD}$–$M_{\rm sec}$ plane is shown in Fig. 10.

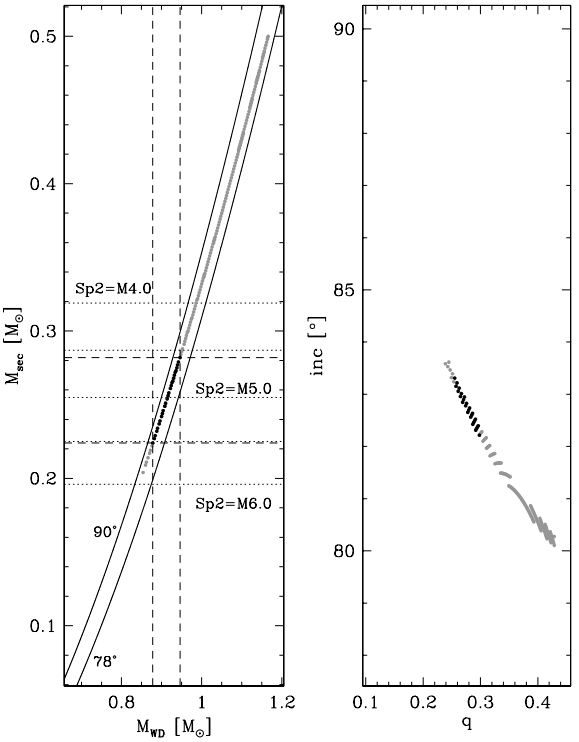

Figure 10. Light-curve model fitting results for SDSS 0303+0054. Left-hand panel: $M_{\rm WD}$ and $M_{\rm sec}$ values corresponding to fits with χ^2 values within 1σ of the minimum value (grey points) and, simultaneously, with $\delta R_{\rm sec} \leq 0.05$ (black points). Right-hand panel: the same, only in the q–i plane. Also depicted in the left-hand panel are curves corresponding to the mass function (solid black lines, $i = 90^\circ$ and 78°) which (by definition) bracket the possible solutions, Sp (2)–$M_{\rm sec}$ relations (dotted, horizontal, black lines) and the range of possible ($M_{\rm WD}$, $M_{\rm sec}$) values (dashed, horizontal and vertical, black lines).

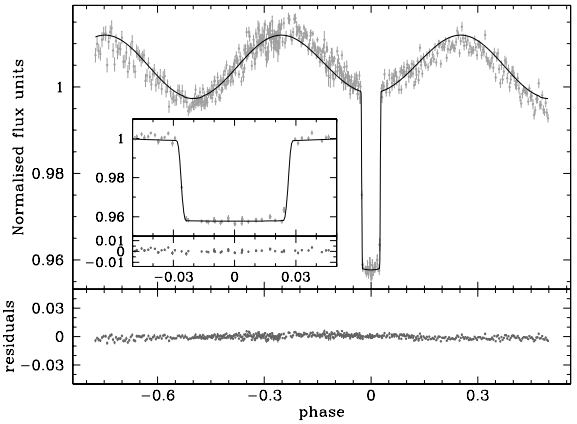

Figure 11. Model fit to the CA2.2 filterless light curve of SDSS 0303+0054, for $M_{\rm WD} = 0.91\,{\rm M}_{\odot}$, $R_{\rm WD} = 0.009\,{\rm R}_{\odot}$, $M_{\rm sec} = 0.25\,{\rm M}_{\odot}$, $R_{\rm sec} = 0.26\,{\rm R}_{\odot}$ and $i = 82.6^{\circ}$. The model meets both our χ^2 (within 1σ) and the δR (within 5 per cent) cut-offs. The residuals from the fit are shown at the bottom of the panel. Inset panel: data points and model fit focused around the eclipse.

Grey dots designate those light-curve fits making the 1σ cut, black dots those that satisfy both the 1σ and $\delta R_{\rm sec} = 5$ per cent cuts. The resulting ranges in white dwarf masses and secondary star masses are $M_{\rm WD,lcfit} = 0.88$–$0.95\,{\rm M}_{\odot}$ and $M_{\rm sec} = 0.22$–$0.28\,{\rm M}_{\odot}$, respectively, corresponding to a white dwarf radius of $R_{\rm WD} = 0.008$–$0.009\,{\rm R}_{\odot}$ and a secondary radius of $R_{\rm sec} = 0.25$–$0.27\,{\rm R}_{\odot}$. Fig. 11 shows one example of the light-curve fits within this range for the model parameters $M_{\rm WD} = 0.91\,{\rm M}_{\odot}$, $R_{\rm WD} = 0.009\,{\rm R}_{\odot}$, $M_{\rm sec} = 0.25\,{\rm M}_{\odot}$, $R_{\rm sec} = 0.26\,{\rm R}_{\odot}$ and $i = 82.6^{\circ}$.

To check the consistency of our light-curve fits with the results from the spectral decomposition, we indicate in Fig. 10 the radii of M dwarfs with spectral types Sp (2) = M 4–M 6 in steps of 0.5, based on the spectral type–mass relation given by Rebassa-Mansergas et al. (2007). The secondary star mass from the light-curve fit, $M_{\rm sec,lcfit} = 0.23$–$0.28\,{\rm M}_{\odot}$, corresponds to a secondary spectral type of Sp $(2)_{\rm lcfit}$ = M 4.5– M 5.5. The expected spectral type of the secondary from the spectral decomposition (Section 6) was ${\rm Sp}_{\rm spfit}(2) = {\rm M}\,4.5 \pm 0.5$, hence, both methods yield consistent results.

9.2 SDSS 1435+3733

For SDSS 1435+3733, which is partially eclipsing, our temporal resolution, although again not ideal, was nevertheless deemed to be adequate to constrain the white dwarf radius from the light-curve fits. Thus, a $\delta R_{\rm WD}$ cut was also applied.

We applied again our strictest cuts on the light-curve models, 1σ and $\delta R_{\rm WD} = \delta R_{\rm sec} = 5$ per cent, and the parameters of the surviving models are shown in Fig. 12, where the meaning of the symbols is the same as in Fig. 10.

These fits imply a white dwarf mass and radius of $M_{\rm WD} = 0.48$–$0.53\,{\rm M}_{\odot}$ and $R_{\rm WD} = 0.014$–$0.015\,{\rm R}_{\odot}$, respectively, and a secondary star mass and radius of $M_{\rm sec} = 0.19$–$0.25\,{\rm M}_{\odot}$ and $R_{\rm sec} = 0.22$–$0.25\,{\rm R}_{\odot}$, respectively. A sample fit that obeyed all three constraints is shown in Fig. 13. The model parameters are $M_{\rm WD} = 0.5\,{\rm M}_{\odot}$, $R_{\rm WD} = 0.015\,{\rm R}_{\odot}$, $M_{\rm sec} = 0.21\,{\rm M}_{\odot}$, $R_{\rm sec} = 0.23\,{\rm R}_{\odot}$ and $i = 77.6^{\circ}$.

Comparing the white dwarf masses from the spectroscopic decomposition/fit, $M_{\rm WD,spfit} = 0.41 \pm 0.08\,{\rm M}_{\odot}$, with the range of white dwarf masses allowed by the light-curve fitting,

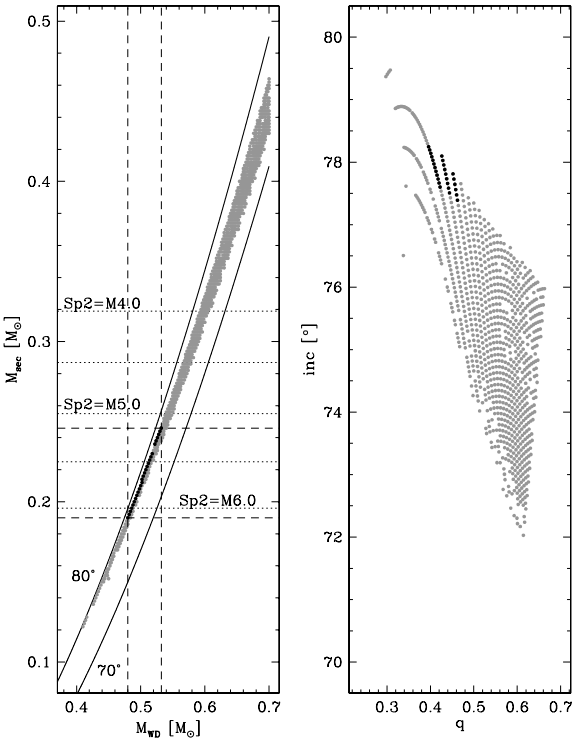

Figure 12. Light-curve model fitting results for SDSS 1435+3733. Left-hand panel: $M_{\rm WD}$ and $M_{\rm sec}$ values corresponding to fits with χ^2 values within 1σ of the minimum value (grey points) and, simultaneously for both white dwarf and secondary radii, with $\delta R \leq 0.05$ (black points). Right-hand panel: the same, only in the q–i plane. Also depicted in the left-hand panel are mass functions ($i = 70^{\circ}$ and 80°, solid black lines), Sp (2)–$M_{\rm sec}$ relations (dotted, horizontal, black lines) and the range of possible ($M_{\rm WD}$, $M_{\rm sec}$) values (dashed, horizontal and vertical, black lines).

$M_{\rm WD,lcfit} = 0.48$–$0.53\,{\rm M}_{\odot}$, reveals a reasonable agreement. Regarding the spectral type of the secondary star, we indicate in Fig. 12 again the masses of M dwarfs in the range M4–M6, in steps of 0.5 spectral classes, following the Sp (2)–$M_{\rm sec}$ relation of Rebassa-Mansergas et al. (2007). This illustrates that the light-curve fits result in a Sp $(2)_{\rm lcfit}$ = M 5–M 6, whereas the spectral decomposition provided Sp $(2)_{\rm spfit}$ = M 4.5 ± 0.5. Hence, also the results for the secondary star appear broadly consistent.

Steinfadt et al. (2008) first reported the eclipsing nature of SDSS 1435+3733, and estimated $M_{\rm WD} = 0.35$–$0.58\,{\rm M}_{\odot}$, $R_{\rm WD} = 0.0132$– $0.0178\,{\rm R}_{\odot}$, $M_{\rm sec} = 0.15$–$0.35\,{\rm M}_{\odot}$ and $R_{\rm sec} = 0.17$–$0.32\,{\rm R}_{\odot}$. The parameter ranges determined from our analysis ($M_{\rm WD} = 0.48$–$0.53\,{\rm M}_{\odot}$, $R_{\rm WD} = 0.014$–$0.015\,{\rm R}_{\odot}$, $M_{\rm sec} = 0.19$–$0.25\,{\rm M}_{\odot}$ and $R_{\rm sec} = 0.22$– $0.25\,{\rm R}_{\odot}$) are fully consistent with Steinfadt et al.'s work. In Fig. 14 we overplot on the photometry of Steinfadt et al. (2008) the light-curve model shown in Fig. 13 along with our data, illustrating that our solution is consistent with their data.

While the temporal resolution of our photometry is worse than that of Steinfadt et al. (2008), our analysis benefited from two additional constraints, first the mass function (equation 9) determined from our spectroscopy, and secondly the detection of a weak ellipsoidal modulation in our *I*-band light curve (Fig. 13). While the observations of Steinfadt et al. (2008) covered the entire binary orbit, their data were obtained through a BG-39 filter, centred at 4800 Å, where the flux contribution of the companion star is negligible. A well-established difficulty in modelling light curves of

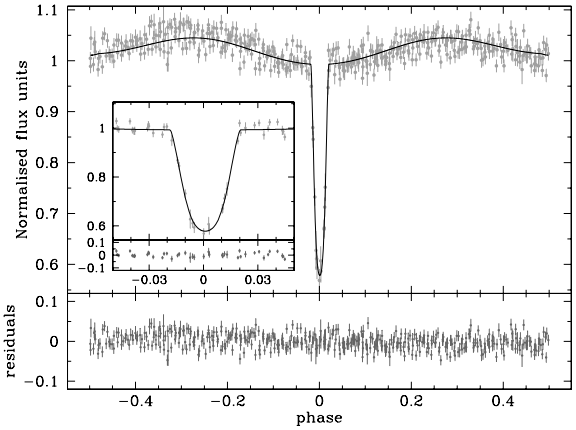

Figure 13. Model fit to IAC80 *I*-band light curve of SDSS 1435+3733, for $M_{\rm WD} = 0.5\,{\rm M}_{\odot}, R_{\rm WD} = 0.015\,{\rm R}_{\odot}, M_{\rm sec} = 0.21\,{\rm M}_{\odot}, R_{\rm sec} = 0.23\,{\rm R}_{\odot}$ and $i = 77.6^{\circ}$. The model meets both the 1σ cut in χ^2, and a $\delta R \leq 0.05$ cut for both the white dwarf and the secondary star. The residuals from the fit are shown at the bottom of the panel. Inset panel: data points and model fit focused around the eclipse.

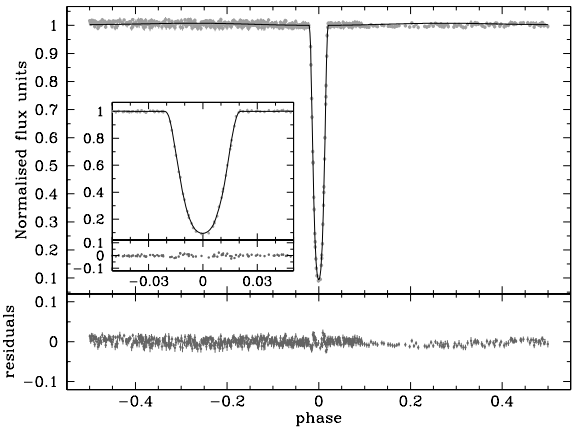

Figure 14. Our light-curve model for SDSS 1435+3733, as determined from fitting our IAC80 *I*-band photometry as shown in Fig. 13, along with the data from Steinfadt et al. (2008), illustrating a high degree of consistency.

partially eclipsing binary stars is the fact that, although the sum of the two radii can be accurately defined, their ratio can only be loosely constrained (e.g. Southworth, Bruntt & Buzasi 2007). $R_{\rm WD}$ and $R_{\rm sec}$ are strongly correlated, and fitting both of them leads to degeneracy. Additional information is needed to lift this degeneracy, which is mainly provided by ellipsoidal modulation or reflection effects (e.g. Hilditch, Harries & Bell 1996a; Hilditch, Harries & Hill 1996b).

9.3 SDSS 1548+4057

For SDSS 1548+4057, we follow a very similar approach as for SDSS 1435+3733, adopting a 1σ cut in χ^2 but a slightly less strict cut on the radii, $\delta R_{\rm WD} = \delta R_{\rm sec} = 10$ per cent. Fig. 15 shows the solutions of our light-curve fits that survived those criteria, where plot symbols have the same meaning as in Figs 10 and 12.

The models satisfying both cuts imply a white dwarf mass and radius of $M_{\rm WD} = 0.61$–$0.68\,{\rm M}_{\odot}$ and $R_{\rm WD} = 0.010$–$0.011\,{\rm R}_{\odot}$, respectively, and a secondary mass and radius of $M_{\rm sec} = 0.15$–$0.20\,{\rm M}_{\odot}$ and $R_{\rm sec} = 0.17$–$0.20\,{\rm R}_{\odot}$, respectively. A sample fit, that

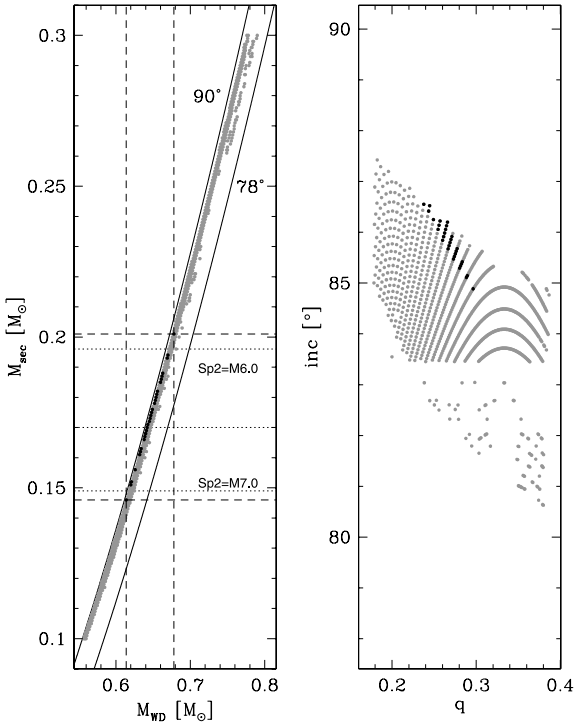

Figure 15. Light-curve model fitting results for SDSS 1548+4057. Left-hand panel: $M_{\rm WD}$ and $M_{\rm sec}$ values corresponding to fits with χ^2 values within 1σ of the minimum value (grey points) and, simultaneously for both white dwarf and secondary radii, with $\delta R \leq 0.1$ (black points). Right-hand panel: the same, only in the q–i plane. Also depicted in the left-hand panel are mass function for $i = 78^{\circ}$ and 90° (solid black lines), Sp (2)–$M_{\rm sec}$ relations for spectral types M6, 6.5 and 7 (dotted, horizontal, black lines) and the range of possible ($M_{\rm WD}$, $M_{\rm sec}$) values (dashed, horizontal and vertical, black lines).

obeyed all three constraints, is shown in Fig. 16. The model parameters are $M_{\rm WD} = 0.65\,{\rm M}_{\odot}, R_{\rm WD} = 0.011\,{\rm R}_{\odot}, M_{\rm sec} = 0.18\,{\rm M}_{\odot}$, $R_{\rm sec} = 0.18\,{\rm R}_{\odot}$ and $i = 85.6^{\circ}$.

The white dwarf parameters obtained from the light-curve fitting are in full agreement with those derived from the spectral decomposition. The former give a possible range of white dwarf masses of $M_{\rm WD,lcfit} = 0.61$–$0.68\,{\rm M}_{\odot}$, while the latter yield a value of $M_{\rm WD,spfit} = 0.62 \pm 0.28\,{\rm M}_{\odot}$. In Fig. 15, we indicate the masses corresponding to secondary spectral types M6, M6.5 and M7. The spectral fitting points to a Sp $(2)_{\rm spfit}$ = M 6 secondary. Our models indicate Sp $(2)_{\rm lcfit}$ = M 6–M 7 again consistent with the spectroscopic result.

9.4 SDSS 0110+1326

Because of the uncertainty in the true $K_{\rm sec}$ velocity of the secondary star, we inspected a total of six different grids of light-curve fits for SDSS 0110+1326 (three *K*-corrections for each of the observed $K_{\rm sec,\,H\alpha}$ and $K_{\rm sec,\,Ca\,II}$, see Section 8.2 and Table 7), and consequently, this star needs a slightly more extensive discussion compared to the other three systems.

In a first exploratory step, we applied our least strict cut-offs, adopting a 3σ cut on the fit quality, and a $\delta R = 15$ per cent cut for both the white dwarf and the secondary star radii. Even with these loose constraints, the $\Delta R = R_{\rm sec}$ case, i.e. assuming that the emission is concentrated on the surface of the secondary closest to the white dwarf, does not produce any solutions that meet the cut-off

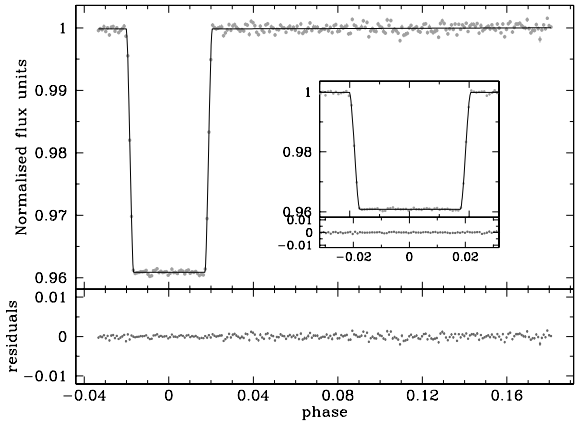

Figure 16. Model fit to the WHT/*R*-band light curve of SDSS 1548+4057, for $M_{\rm WD} = 0.65\,{\rm M}_{\odot}$, $R_{\rm WD} = 0.011\,{\rm R}_{\odot}$, $M_{\rm sec} = 0.18\,{\rm M}_{\odot}$, $R_{\rm sec} = 0.183\,{\rm R}_{\odot}$ and $i = 86.6^{\circ}$. The model meets both a 1σ χ^2 cut-off, and the $\delta R \leq 0.10$, cut-off, for both the white dwarf and the secondary radii. The residuals from the fit are shown at the bottom of the panel. Inset panel: data points and model fit focused around the eclipse.

Table 7. Summary of the fitting results of SDSS 0110+1326, for all three ΔR prescriptions, for both the cases of the H α and the Ca II emission lines. In all cases we applied 3σ and $\delta R = 15$ per cent cut-offs. A ($\surd$) means some models passed the cut-off, whereas a (–) means no models passed.

	Hα	Ca II
$\Delta R = 0$	$\surd$	$\surd$
$\Delta R = (4/3\pi)R_{\rm sec}$	–	$\surd$
$\Delta R = R_{\rm sec}$	–	–

criteria. For the uniform illumination case, $\Delta R = (4/3\pi)R_{\rm sec}$, there were no solutions for $K_{\rm sec} = K_{\rm sec,\,H\alpha}$, but a few solutions for the $K_{\rm sec} = K_{\rm sec,\,Ca\,II}$. Finally, a number of solutions existed for the case $\Delta R = 0$, i.e. assuming no *K*-correction, for both Hα and Ca II. Table 7 summarizes this analysis, and the models that survived the culling defined ranges of $(M_{\rm WD}, M_{\rm sec})$ pairs which are illustrated in Fig. 17.

Given that the uniform irradiation prescription, $\Delta R = (4/3\pi)R_{\rm sec}$ represents a mid-way between the two extreme assumptions $\Delta R = R_{\rm sec}$ and $\Delta R = 0$, and that a reasonably large range of possible solutions was found for the Ca II velocities (Fig. 17), we decided to explore tighter χ^2 constraints for this case. While a number of light-curve models are found within 1σ of the minimum χ^2 value, both $\delta R_{\rm WD}$ and $\delta R_{\rm sec}$ were $\sim$15 per cent in all cases. No models survived if we reduced the value of δR in addition to the tighter χ^2 constraint.

As an illustration of the quality of the light-curve fits achieved, Fig. 18 shows a fit with $M_{\rm WD} = 0.59\,{\rm M}_{\odot}$, $R_{\rm WD} = 0.015\,{\rm R}_{\odot}$, $M_{\rm sec} = 0.28\,{\rm M}_{\odot}$, $R_{\rm sec} = 0.32\,{\rm R}_{\odot}$, $i = 85^{\circ}$ and $K_{\rm sec} = 197\,{\rm km\,s^{-1}}$. The mass of the secondary corresponds to a spectral type of Sp (2) = M 4.5. We stress, however, that we do not adopt this model as a final solution for the parameters of SDSS 0110+1326, but rather consider it as a physically plausible set of parameters.

Taking the 1σ confidence levels of the light-curve fits at face value, they imply a white dwarf mass of $M_{\rm WD,lcfit} = 0.59$–$0.7\,{\rm M}_{\odot}$ and a secondary mass of $M_{\rm sec,lcfit} = 0.28$–$0.38\,{\rm M}_{\odot}$.

For the white dwarf, these numbers are in contrast with the results from the spectral decomposition, $M_{\rm WD,spfit} = 0.47 \pm 0.02\,{\rm M}_{\odot}$.

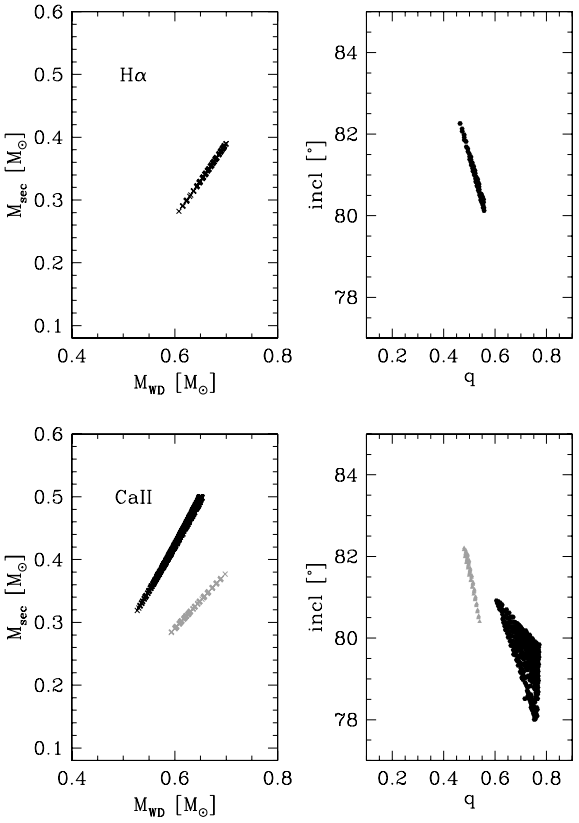

Figure 17. Results of the model fitting of SDSS 0110+1326 for H α (left-hand panels) and Ca II (right-hand panels), for a 3σ confidence level and $\delta R < 0.15$. Black points correspond to $\Delta R = 0$, grey to $\Delta R = (4/3\pi)R_{\rm sec}$ (where applicable, see text for details). Top panels show the $(M_{\rm WD}, M_{\rm sec})$ plain, bottom panels the *q*–*i* plain.

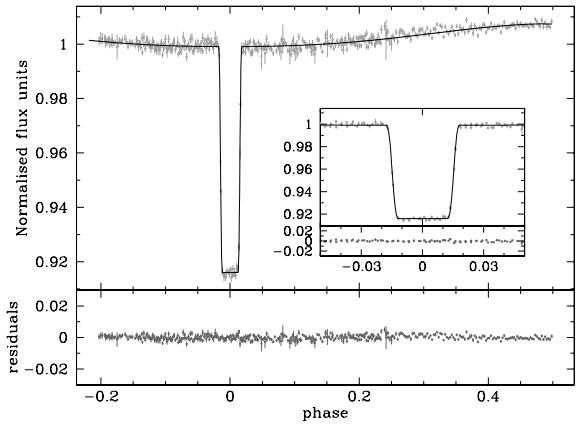

Figure 18. Model fit to the CA2.2 *I*-band light curve of SDSS 0110+1326, for $M_{\rm WD} = 0.59\,{\rm M}_{\odot}$, $R_{\rm WD} = 0.015\,{\rm R}_{\odot}$, $M_{\rm sec} = 0.28\,{\rm M}_{\odot}$, $R_{\rm sec} = 0.32\,{\rm R}_{\odot}$ $i = 85^{\circ}$ and $K_{\rm sec} = 197\,{\rm km\,s^{-1}}$. The model radii agree with the theoretically predicted ones within 15 per cent, for both the white dwarf and the secondary star. The residuals from the fit are shown at the bottom of the panel. Inset panel: data points and model fit focused around the eclipse.

The errors in the spectroscopic white dwarf parameters are purely of statistical nature. However, even assuming a reasonably large systematic error of 0.2 dex in $\log g$ (implying $M_{\rm WD,spfit} = 0.39$–$0.55\,{\rm M}_{\odot}$) the white dwarf masses implied by the light-curve fit and the spectroscopic fit appear to be inconsistent.

Table 8. Reconstructed and predicted orbital periods as well as expected evolutionary times for the four new eclipsing WDMS binaries. The cooling age of the white dwarfs is $t_{\rm cool}$ while $P_{\rm CE}$ and $P_{\rm sd}$ are the orbital periods at the end of the CE phase and at the onset of mass transfer, respectively. The time still needed to enter the semidetached CV configuration is $t_{\rm sd}$.

SDSS J	$t_{\rm cool}$ (yr)	$P_{\rm sd}$ (d)	$P_{\rm CE}$ (d)	$t_{\rm sd}$ (yr)
0110+1326	1.41e+07	0.097	0.332	1.78e+10
1548+4057	3.91e+08	0.069	0.191	4.23e+09
0303+0054	3.23e+09	0.097	0.228	5.95e+08
1435+3733	2.53e+08	0.088	0.132	9.50e+08

Regarding the secondary, adopting $M_{\rm sec,lcfit} = 0.28$–$0.38\,{\rm M}_{\odot}$ and the Sp (2)–$M_{\rm sec}$ relation of Rebassa-Mansergas et al. (2007) suggests a spectral type of Sp $(2)_{\rm lcfit}$ = M 3–M 4.5, which is consistent with the results of the spectral decomposition, Sp $(2)_{\rm spfit}$ = M 4 ± 1.

While our analysis of the light-curve fits demonstrates that the data can be modelled well, it is clear that the lack of a reliable value for $K_{\rm sec}$ prevents the choice of the physically most meaningful solution. Consequently, a definite determination of the stellar parameters of SDSS 0110+1326 is not possible on the basis of the currently available data, and we adopt as a first cautious estimate the values of our spectral decomposition fit. As mentioned in Section 8.2, a physically motivated K-correction can be modelled once a larger set of spectra covering the entire binary orbit are available.

10 POST-COMMON-ENVELOPE EVOLUTION

Considering their short orbital periods, the four new eclipsing WDMS binaries discussed in this paper must have formed through CE evolution (Paczynski 1976; Webbink 2007). Post-common-envelope binaries (PCEBs) consisting of a white dwarf and a main-sequence star evolve towards shorter orbital periods by angular momentum loss through gravitational radiation and magnetic braking until they enter the semidetached CV configuration. As shown by Schreiber & Gänsicke (2003), if the binary and stellar parameters are known, it is possible to reconstruct the past and predict the future evolution of PCEBs for a given angular momentum loss prescription. Here, we assume classical disrupted magnetic braking (Rappaport, Joss & Verbunt 1983), i.e. magnetic braking is supposed to be much more efficient than gravitational radiation but only present as long as the secondary star has a radiative core. For fully convective stars gravitational radiation is assumed to be the only angular momentum loss mechanism, which applies to all four systems. The current ages of the PCEBs are determined by interpolating the cooling tracks from Wood, Naylor & Marsh (1995a). Table 8 lists the evolutionary parameters for our four eclipsing WDMS binaries.

The calculated evolutionary tracks of the four systems are shown in Fig. 19. The present position of each binary is indicated by an asterisk. The grey-shaded region indicates the 2–3 h orbital period gap, i.e. the orbital period range where only a small number of CVs has been found. Given that the four WDMS binaries contain low-mass secondary stars, all of them are expected to start mass transfer in or below the period gap. This underlines the fact first noticed by Schreiber & Gäensicke (2003) that only very few progenitors of long-period CVs are known. SDSS 0303+0054 has passed most of its PCEB lifetime and its current orbital period differs significantly from the reconstructed value at the end of the CE phase. The other three systems are rather young PCEBs with a current orbital period close to $P_{\rm CE}$.

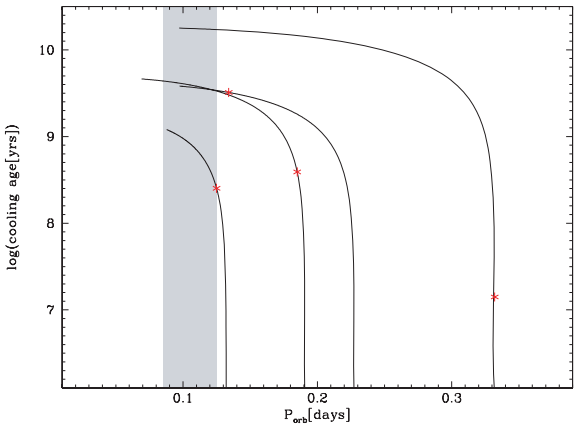

Figure 19. Evolutionary post-common-envelope tracks for our four eclipsing binaries. From left to right: SDSS 1435+3733, SDSS 1548+4057, SDSS 0303+0054 and SDSS 0110+1326. The current position of the systems is indicated by an asterisk. We assumed only gravitational wave radiation as angular momentum loss agent as all four systems are thought to contain fully convective secondary stars. The orbital period gap of CVs is highlighted in grey – all four systems will start mass transfer in, or shortly below the gap.

11 CONCLUSIONS

Since Nelson & Young (1970) reported the discovery of V471 Tau, as the first eclipsing WDMS binary, only seven additional similar systems have been discovered, the latest being SDSS 1435+3733 found by Steinfadt et al. (2008). Here, we presented follow-up observations of SDSS 1435+3733, which we independently identified as an eclipsing WDMS binary, and of three new discoveries: SDSS 0110+1326, SDSS 0303+0050 and SDSS 1548+4057. A fifth system has just been announced by our team (Nebot Gómez-Morán et al. 2008), and two eclipsing WDMS binaries were identified by Drake et al. (2008) in the Catalina Real-Time Transient Survey. Table 9 lists the basic physical parameters of the 14 eclipsing WDMS binaries currently known.

Inspection of Table 9 shows that the orbital periods of the known eclipsing binaries range from 3 to 12 h, with three of the systems presented here settling in at the short-period end.

The white dwarf masses cover a range ∼0.44–0.9 $\rm M_{\odot}$, with an average of $\langle M_{\rm WD}\rangle = 0.57 \pm 0.16\,{\rm M}_{\odot}$, which is only slightly lower than the average mass of single white dwarfs (Koester et al. 1979; Finley, Koester & Basri 1997; Liebert et al. 2005). This finding is somewhat surprising, as all these eclipsing WDMS binaries have undergone a CE evolution, which is expected to cut short the evolution of the primary star and thereby to produce a significant number of low-mass He-core white dwarfs. Our estimates for the white dwarf masses in SDSS 0110+1326 and SDSS 1435+3733 suggest that they contain He-core white dwarfs. The white dwarf in SDSS 1548+4057 is consistent with the average mass of single white dwarfs. SDSS 0303+0054 contains a fairly massive white dwarf, potentially the most massive one in an eclipsing WDMS binary.

The secondary star masses are concentrated at very low masses, the majority of the 14 systems in Table 9 have $M_{\rm sec} < 0.6\,{\rm M}_{\odot}$, and ∼nine systems (including the four stars discussed here) have $M_{\rm sec} \lesssim 0.3\,{\rm M}_{\odot}$. This is a range where very few low-mass stars in eclipsing

Table 9. Physical parameters of the known eclipsing WDMS binaries. A dash sign means that no corresponding value was given by the respective authors. Errors on the parameters are also shown, if quoted by the authors.

System	$P_{\rm orb}$ (d)	$M_{\rm WD}$ ($M_\odot$)	$R_{\rm WD}$ ($R_\odot$)	$T_{\rm eff,WD}$ (K)	$\log g$	$M_{\rm sec}$ ($M_\odot$)	$R_{\rm sec}$ ($R_\odot$)	$K_{\rm WD}$ (km s^{-1})	$K_{\rm sec}$ (km s^{-1})	Sp2	Ref.
V471 Tau	0.521	0.79	0.01	32 000	–	0.8	0.85	–	150.7 ± 1.2	K2	1a
	0.521	0.84 ± 0.05	0.0107 ± 0.0007	34 500 ± 1000	8.31 ± 0.06	0.93 ± 0.07	0.96 ± 0.04	163.6 ± 3.5	148.46 ± 0.56	K2	1b
RX J2130.6+4710	0.521	0.554 ± 0.017	0.0137 ± 0.0014	18 000 ± 1000	$7.93^{+0.07}_{-0.09}$	0.555 ± 0.023	0.534 ± 0.017	136.5 ± 3.8	136.4 ± 0.8	M3.5–M4	2
DE CVn	0.364	$0.51^{+0.06}_{-0.02}$	$0.0136^{+0.0008}_{-0.0002}$	8000 ± 1000	7.5	0.41 ± 0.06	$0.37^{+0.06}_{-0.007}$	–	166 ± 4	M3V	3
GK Vir	0.344	0.7 ± 0.3	–	50 000	–	–	–	–	–	M0–M6	4a
	0.344	0.51 ± 0.04	0.016	48 800 ± 1200	7.7 ± 0.11	0.1	0.15	–	–	M3–M5	4b
SDSS 1212−0123	0.335	0.46–0.48	0.016–0.018	17 700 ± 300	7.5–7.7	0.26–0.29	0.28–0.31	–	181 ± 3	M4 ± 1	5
SDSS 0110+1326	0.332	0.47 ± 0.2	0.0163–0.0175	25 900 ± 427	7.65 ± 0.05	0.255–0.38	0.262–0.36	–	180-200	M3–M5	6
RR Cae	0.303	0.365	0.0162	7000	–	0.089	0.134	47.9[a]	195.8*	M6	7a
	0.303	0.467	0.0152	7000	–	0.095	0.189	–	190 ± 9	M6	7b
	0.303	0.44 ± 0.022	0.015 ± 0.0004	7540 ± 175	7.61–7.78	0.183 ± 0.013	0.188–0.23	79.3 ± 3	190.2 ± 3.5	M4	7c
SDSS 1548+4057	0.185	0.614–0.678	0.0107–0.0116	11 700 ± 820	8.02 ± 0.44	0.146–0.201	0.166–0.196	–	274.7	M5.5–M6.5	6
EC 13471−1258	0.150	0.77 ± 0.04	–	14 085 ± 100	8.25 ± 0.05	0.58 ± 0.05	0.42 ± 0.08	–	241 ± 8.1	M2–M4	8a
	0.150	0.78 ± 0.04	0.011 ± 0.01	14 220 ± 300	8.34 ± 0.2	0.43 ± 0.04	0.42 ± 0.02	138 ± 10	266 ± 5	M3.5–M4	8b
CSS 080502[b]	0.149	0.35 ± 0.04	0.02 ± 0.002	17 505 ± 516	7.38 ± 0.12	0.32	0.33	–	–	M4	6, 9
SDSS 0303+0054	0.134	0.878–0.946	0.0085–0.0093	< 8000	8.4–8.6	0.224–0.282	0.246–0.27	–	339.7	M4–M5	6
NN Ser	0.130	0.57 ± 0.04	0.017–0.021	55 000 ± 8000	7–8	0.10–0.14	0.15–0.18	–	310 ± 10	M4.7–M6.1	10a,b
	0.130	0.54 ± 0.05	0.0189 ± 0.001	57 000 ± 3000	7.6 ± 0.1	0.15 ± 0.008	0.174 ± 0.009	80.4 ± 4.1	289.3 ± 12.9	M4.5–M5	10c
SDSS 1435+3733	0.125	–	–	–	–	0.15–0.35	0.17–0.32	–	–	M4–M6	11
	0.125	0.48–0.53	0.0144–0.0153	12 500 ± 488	7.62 ± 0.12	0.19–0.246	0.218–0.244	–	260.9	M4–M5	6
CSS 080408[c]	–	0.40 ± 0.05	0.022 ± 0.003	32 595 ± 675	7.36 ± 0.17	0.26	0.27	–	–	M5	6, 9

Ref.: 1a – Young & Nelson (1972); 1b – O'Brien et al. (2001); 2 – Maxted et al. (2004); 3 – van den Besselaar et al. (2007); 4a – Green, Richstone & Schmidt (1978); 4b – Fulbright et al. (1993); 5 – Nebot Gómez-Morán et al. (2008); 6 – this work; 7a – Bruch & Diaz (1998); 7b – Bruch (1999); 7c – Maxted et al. (2007); 8a – Kawka et al. (2002); 8b – O'Donoghue et al. (2003); 9 – Drake et al. (2008); 10a – Wood & Marsh (1991); 10b – Catalan et al. (1994); 10c – Haefner et al. (2004); 11 – Steinfadt et al. (2008).

[a]Calculated from $K \sin i$ provided by the authors.

[b]CSS 080502:090812+060421 = SDSS J090812.04+060421.2, we determined the white dwarf and secondary star parameters from decomposing/fitting the SDSS spectrum (see Section 6 and Rebassa-Mansergas et al. 2007), these parameters should be taken as guidance as no light-curve modelling has been done so far.

[c]CSS 080408:142355+240925 = SDSS J142355.06+240924.3, also found by Rebassa-Mansergas et al. (in preparation), white dwarf and secondary star parameters determined as for CSS 080502.

binaries are known (Ribas 2006), making the secondary stars in eclipsing WDMS binaries very valuable candidates for filling in the empirical mass–radius relation of low-mass stars. This aspect will be discussed in a forthcoming paper.

The distribution of secondary star masses among the eclipsing PCEBs in Table 9 is subject to similar selection effects as the whole sample of known PCEBs. Schreiber & Gänsicke (2003) found a strong bias towards late-type secondary stars in the pre-SDSS PCEB population, which arose as most of those PCEBs were identified in blue-colour surveys. The currently emerging population of SDSS PCEBs (Silvestri et al. 2006; Rebassa-Mansergas et al., in preparation) should be less biased as the *ugriz* –colour space allows to identify WDMS binaries with a wide range of secondary spectral types and white dwarf temperatures.

Future work will need to be carried out on two fronts. On one hand, more accurate determination of the masses and radii will have to be made to unlock the potential that WDMS binaries hold for testing/constraining the mass–radius relation of both white dwarfs and low-mass stars. The key to this improvement are high-quality light curves that fully resolve the white dwarf ingress/egress, and, if possible, the secondary eclipse of the M dwarf by the white dwarf. In addition, accurate $K_{\rm WD}$ velocities are needed, which will be most reliably obtained from ultraviolet intermediate resolution spectroscopy. On the other hand, it is clear that the potential of SDSS in leading to the identification of additional eclipsing WDMS binaries has not been exhausted. Additional systems will be identified by the forthcoming time-domain surveys, and hence growing the class of eclipsing WDMS binaries to several dozen seems entirely feasible.

ACKNOWLEDGMENTS

We thank Justin Steinfadt for providing his light-curve data on SDSS 1435+3733 and the referee, P. Maxted, for his useful comments and suggestions. MRS acknowledges support from FONDECYT (grant 1061199), DIPUV (project 35), the Centre of Astrophysics in Valparaiso, and Basel CATA PFB 06/09. Based in part on observations made with the WHT, operated on the island of La Palma by the Isaac Newton Group, in the Spanish Observatorio del Roque de los Muchachos of the Instituto de Astrofísica de Canarias; on observations made with the NOT, operated on the island of La Palma jointly by Denmark, Finland, Iceland, Norway and Sweden, in the Spanish Observatorio del Roque de los Muchachos of the Instituto de Astrofísica de Canarias; on observations collected at the Centro Astronómico Hispano Alemán (CAHA) at Calar Alto operated jointly by the Max-Planck Institut für Astronomie and the Instituto de Astrofísica de Andalucía (CSIC); on observations made with the MER, operated on the island of La Palma by the Flemish Community, in the Spanish Observatorio del Roque de los Muchachos of the Instituto de Astrofísica de Canarias and on observations made with the IAC80 telescope, operated by the Instituto de Astrofísica de Canarias, in the Observatorio del Teide.

REFERENCES

Andersen J., 1991, ARA&A, 3, 91
Baraffe I., Chabrier G., Allard F., Hauschildt P. H., 1998, A&A, 337, 403
Bayless A. J., Orosz J. A., 2006, ApJ, 651, 1155
Berger D. H. et al., 2006, ApJ, 644, 475
Bergeron P., Wesemael F., Beauchamp A., 1995, PASP, 107, 1047
Bertin E., Arnouts S., 1996, A&AS, 117, 393
Bruch A., 1999, AJ, 117, 3031
Bruch A., Diaz M. P., 1998, AJ, 116, 908
Catalan M. S., Davey S. C., Sarna M. J., Connon-Smith R., Wood J. H., 1994, MNRAS, 269, 879
Dorman B., Nelson L. A., Chau W. Y., 1989, ApJ, 342, 1003
Drake A. J. et al., 2008, ApJ, submitted (arXiv:0809.1394)
Finley D. S., Koester D., Basri G., 1997, ApJ, 488, 375
Fulbright M. S., Liebert J., Bergeron P., Green R., 1993, ApJ, 406, 240
Gänsicke B. T., Araujo-Betancor S., Hagen H.-J., Harlaftis E. T., Kitsionas S., Dreizler S., Engels D., 2004, A&A, 418, 265
Green R. F., Richstone D. O., Schmidt M., 1978, ApJ, 224, 892
Haefner R., Fiedler A., Butler K., Barwig H., 2004, A&A, 428, 181
Hilditch R. W., Harries T. J., Bell S. A., 1996a, A&A, 314, 165
Hilditch R. W., Harries T. J., Hill G., 1996b, MNRAS, 279, 1380
Horne K., 1986, PASP, 98, 609
Kawka A., Vennes S., 2003, AJ, 125, 1444
Kawka A., Vennes S., Koch R., Williams A., 2002, AJ, 124, 2853
Kawka A., Vennes S., Dupuis J., Chayer P., Lanz T., 2007, ApJ, 675, 1518
Koester D., Schulz H., Weidemann V., 1979, A&A, 76, 262
Koester D., Napiwotzki R., Voss B., Homeier D., Reimers D., 2005, A&A, 439, 317
Liebert J., Bergeron P., Holberg J. B., 2005, ApJS, 156, 47
López-Morales M., 2007, ApJ, 660, 732
Marsh T. R., 1989, PASP, 101, 1032
Maxted P. F. L., Marsh T. R., Moran C., Dhillon V. S., Hilditch R. W., 1998, MNRAS, 300, 1225
Maxted P. F. L., Marsh T. R., Morales-Rueda L., Barstow M. A., Dobbie P. D., Schreiber M. R., Dhillon V. S., Brinkworth C. S., 2004, MNRAS, 355, 1143
Maxted P. F. L., O'Donoghue D., Morales-Rueda L., Napiwotzki R., 2007, MNRAS, 376, 919
Morales J. C., Ribas I., Jordi C., 2008, A&A, 478, 507
Nebot Gómez-Morán A. et al., 2008, A&A, accepted (arXiv:0901.2051)
Nelson B., Young A., 1970, PASP, 82, 699
O'Brien M. S., Bond H. E., Sion E. M., 2001, ApJ, 563, 971
O'Donoghue D., Koen C., Kilkenny D., Stobie R. S., Koester D., Bessell M. S., Hambly N., MacGillivray H., 2003, MNRAS, 345, 506
Orosz J. A., Wade R. A., Harlow J. J. B., Thorstensen J. R., Taylor C. J., Eracleous M., 1999, AJ, 117, 1598
Paczynski B., 1976, in Eggleton P., Mitton S., Whelan J., eds, Proc. IAU Symp. 73, Structure and Evolution of Close Binary Systems. Reidel, Dordrecht, p. 75
Panei J. A., Althaus L. G., Benvenuto O. G., 2000, A&A, 353, 970
Provencal J. L., Shipman H. L., Hog E., Thejll P., 1998, ApJ, 494, 759
Rappaport S., Joss P. C., Verbunt F., 1983, ApJ, 275, 713
Rebassa-Mansergas A., Gänsicke B. T., Rodríguez-Gil P., Schreiber M. R., Koester D., 2007, MNRAS, 382, 1377
Rebassa-Mansergas A. et al., 2008, MNRAS, 390, 1635
Ribas I., 2006, Ap&SS, 304, 89
Ribas I., Morales J., Jordi C., Baraffe I., Chabrier G., Gallardo J., 2008, Mem. Soc. Astron. Ital., 79, 562
Schreiber M. R., Gänsicke B. T., 2003, A&A, 406, 305
Schreiber M. R., Gänsicke B. T., Southworth J., Schwope A. D., Koester D., 2008, A&A, 484, 441
Silvestri N. M. et al., 2006, AJ, 131, 1674
Southworth J., Clausen J. V., 2007, A&A, 461, 1077
Southworth J., Gänsicke B. T., Marsh T. R., de Martino D., Hakala P., Littlefair S., Rodríguez-Gil P., Szkody P., 2006, MNRAS, 373, 687
Southworth J., Bruntt H., Buzasi D. L., 2007, A&A, 467, 1215
Southworth J. et al., 2008, MNRAS, 391, 591
Steinfadt J. D. R., Bildsten L., Howell S. B., 2008, ApJ, 677, L113
Tappert C., Gänsicke B. T., Schmidtobreick L., Aungwerojwit A., Mennickent R. E., Koester D., 2007, A&A, 474, 205
Torres G., 2007, ApJ, 671, L65
van den Besselaar E. J. M. et al., 2007, A&A, 466, 1031
Vennes S., Thorstensen J. R., Polomski E. F., 1999, ApJ, 523, 386

Wade R. A., Horne K., 1988, ApJ, 324, 411
Webbink R. F., 2007, in Milone E., Leahy D., Hobill D., eds, Short Period Binary Stars, Vol. 352. Springer-Verlag, Berlin, p. 233
Wood M. A., 1995, in Koester D., Werner K., eds, Lecture Notes in Physics 443, White Dwarfs. Springer-Verlag, Heidelberg, p. 41
Wood J. H., Marsh T. R., 1991, ApJ, 381, 551
Wood J. H., Naylor T., Marsh T. R., 1995a, MNRAS, 274, 31
Wood J. H., Robinson E. L., Zhang E.-H., 1995b, MNRAS, 277, 87
Young A., Nelson B., 1972, ApJ, 173, 653

This paper has been typeset from a TEX/LATEX file prepared by the author.